The magmatic evolution of the Land's End pluton, Cornwall, and associated pre-enrichment of metals

Axel Müller [a,*], Reimar Seltmann [a], Christopher Halls [a], Wolfgang Siebel [b], Peter Dulski [c], Teresa Jeffries [a], John Spratt [a], Andreas Kronz [d]

[a]Natural History Museum, Department. Mineralogy, Cromwell Road, London SW7 5BD, UK
[b]Eberhard Karls Universität Tübingen, Wilhelmstr. 56, D-72074 Tübingen, Germany
[c]GeoForschungsZentrum Potsdam, Telegrafenberg B227, D-14473 Potsdam, Germany
[d]Geowissenschaftliches Zentrum Göttingen, Goldschmidtstr. 3, D-37073 Göttingen, Germany

Abstract

The peraluminous Land's End granite is one of the composite plutons forming the late-Variscan Cornubian batholith. The western part of the pluton hosts the Sn–Cu mineralisation of the St. Just mining district. The pluton consists of early megacrystic biotite (Mg-siderophyllite) granites and albite microgranites and younger Li-siderophyllite granites, and tourmaline granites together with fine-grained massive quartz–tourmaline rocks (MQT). Most of the granite varieties evolved by fractional crystallisation from a common crustal magmatic reservoir, apart from the albite microgranite, which has a different source. Trace element analyses of K-feldspar megacrysts in the older biotite granites made using laser ablation ICP-MS reveal that the megacrysts were derived from moderately evolved sources and now reside in separate granite sub-stages with variable degrees of fractionation, so that equilibrium between phenocrysts and host no longer persists.

The younger granites show a strong in situ fractionation at the cm- to 100-m-scale, whereby boron-rich melts are concentrated in the apical parts of the individual intrusive units. Geological, textural and mineralogical data suggest that the tourmaline granites and MQT evolved mainly from fractionated Li-siderophyllite granites. Cathodoluminescence, trace element and melt inclusion studies of quartz from the MQT reveal that the MQT was formed during the transition from the magmatic to hydrothermal states from a mixture of immiscible phases. The Li-siderophyllite granites, tourmaline granites and MQT appear to be the immediate magmatic precursors from which the hydrothermal fluids responsible for the mineralisation in the St Just district originated.

© 2005 Elsevier B.V. All rights reserved.

Keywords: Land's End granite; Tourmaline; REE; LA-ICP-MS; Cornwall; Peraluminous; Potassium feldspar

* Corresponding author. Present address: Norges Geologiske Undersøkelse, N-7491 Trondheim, Norway. Tel.: +47 73904216; fax: +47 73921620.
   E-mail address: Axel.Muller@ngu.no (A. Müller).

1. Introduction

The Land's End pluton, in which the U–Pb age of monazite has been determined as 277 to 274.5 Ma by Chen et al. (1993), is the youngest of five main granite plutons which form the Cornubian batholith. These are the Dartmoor, Bodmin, St. Austell, Carnmenellis and Land's End granites (Fig. 1). The main cycle of
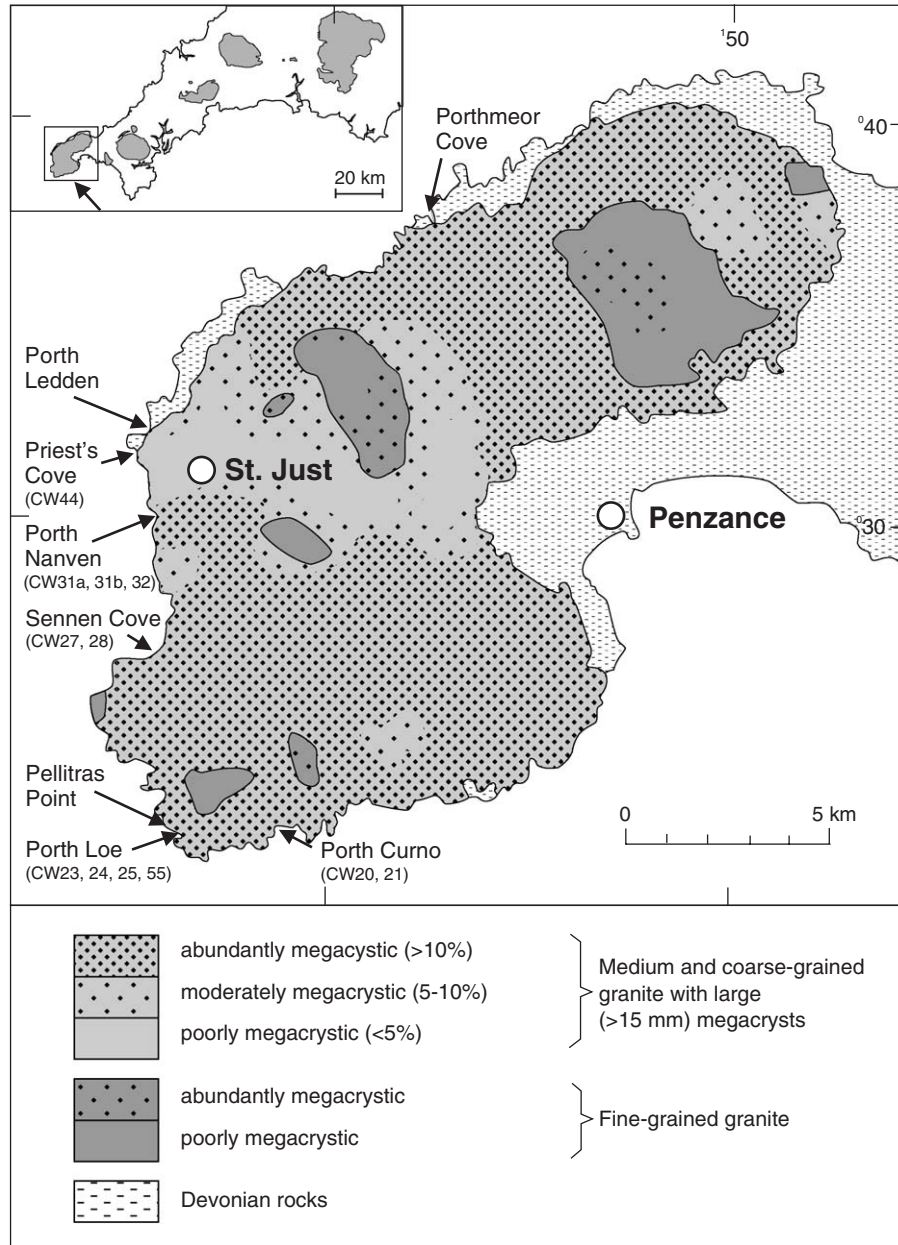

Fig. 1. Distribution of textural variations within the Land's End pluton based on the geological map sheet Penzance 351/358 (British Geological Survey, 1984). The inset shows the location of the Land's End pluton within the Cornubian batholith in SW England. Numbers in parentheses correspond to sample locations. Sampling locations at Porthmeor Cove, Porth Ledden and Pellitras Point are given in more detail in Fig. 2.

metalliferous mineralisation, occurring within and immediately surrounding the five granite plutons in SW England, began with the Variscan cycle of granite plutonism. The Land's End pluton which hosts the Sn–Cu–As mineralisation of the St Just mining district is one of the areas where the concept of the genetic relationship between hydrothermal mineralisation and granite intrusions has been the subject of extensive research (Dines, 1956; Garnett, 1966; Wilson, 1972; Jackson, 1976, 1977, 1979; Alderton and Sheppard, 1977; Charoy, 1979, 1981, 1982; Jackson et al., 1982; Darbyshire and Shepherd, 1985; Mount, 1985; Van Marcke de Lummen, 1986; Halls et al., 2002).

Most of the above studies focus on the pattern of the lodes, the distribution of mineralisation within them and the processes of hydrothermal alteration. A few studies have been concerned with petrographic and textural descriptions of the intrusive units of the Land's End pluton and their relative ages (Stone and Exley, 1984; Salmon, 1994; Salmon and Powell, 1998; Salmon and Shail, 1999; Powell et al., 1999). Van Marcke de Lummen (1986) described many petrographic features of the skarns at the granite contact and gave an overview of the chemical evolution of the Land's End pluton. Wilson (1972), Wilson and Floyd (1974) and Jackson (1977) published analyses of granite units occurring in the St. Just Mining district. Charoy (1979) and Halls et al. (2002) described the field relationships between the outer carapace of megacrystic biotite granites and the inner tourmaline granites and the massive quartz–tourmaline rock (MQT; "tourmalinite") at Porth Ledden, and commented on the sequence of these discrete intrusive events. Geochemical and mineralogical studies of the magmatic evolution of the Land's End pluton have, however, not been well-integrated with the field evidence for the discrete stages of magma placement. This contribution attempts to fill this gap.

Here, a classification of the intrusive stages of the Land's End granite is presented, based on field relationships, magmatic texture, whole-rock and mica composition. Chemical zoning in K-feldspar, quartz, mica, tourmaline and accessory minerals has been analysed and used to interpret the history of crystallisation. The patterns of elements in K-feldspar and quartz phenocryst give information about the early stage of magma evolution. Groundmass quartz and tourmaline provide a record the late-magmatic stage

and, in places, the transition to hydrothermal conditions. Tourmalines from other sites in the Cornubian batholith have been studied by Power (1968), Manning (1985), Farmer and Halls (1993), London and Manning (1995), and Williamson et al. (2000) among others. These investigations showed that the composition of tourmaline changes during the evolution of a granitic system towards the pneumatolytic stage, thus allowing the trend of magmatic differentiation to be tracked.

Optical microscope cathodoluminescence (OM-CL) and scanning electron microscope cathodoluminescence (SEM-CL) have been used to reveal intragranular growth and alteration structures in quartz. Although the physical rationale of the CL phenomena in quartz is not completely understood, the structures revealed by CL provide information about quartz growth in igneous rocks (Sprunt and Nur, 1979; D'Lemos et al., 1997; Watt et al., 1997; Müller et al., 2000, 2003a, 2005). The CL patterns reveal episodes of crystallisation including crystal nucleation and growth and dissolution and different kinds of alteration (post-crystallisation diffusion, healing of deformation structures and intracrystalline fluid pathways). Intra-granular textures of quartz which are often only several μm in scale are best resolved by scanning electron microscope cathodoluminescence (SEM-CL). Optical microscope CL (OM-CL) provides colour information. A combination of these two methods has been used to explain the genesis of the massive quartz–tourmaline rock (MQT) at Porth Ledden. The genesis of the MQT at Porth Ledden is of particular interest because, of all the MQT rocks in Cornwall, its origin appears to be most directly linked to magmatic processes (Badham, 1980; Charoy, 1982; Halls et al., 2002). In contrast, other MQT rocks such as St Mewan's Beacon and Roche Rock are generally considered to be hydrothermal in origin (Collins and Coon, 1914; Bottrell and Yardley, 1988). Finally, the extent to which magmatic differentiation contributed to the pre-enrichment of metals responsible for the Sn–Cu mineralisation around the 'emanative centre' of St Just is assessed.

2. Field setting and petrographic description

The Land's End pluton intrudes Devonian metasediments and associated metavolcanics of the Mylor

formation (Goode and Taylor, 1988). The mineralogical composition and petrographic features of the main intrusive units of the Land's End pluton are given in Table 1. The field relations at the key localities at Porthmeor Cove, Porth Ledden, Priest's Cove, Porth Loe and Pellitras Point are described in more detail below (Fig. 2).

At *Porthmeor Cove* two small intrusions, with associated veins and dykes, and the contact between the main pluton and Devonian metabasites are exposed. The more northern intrusion is inaccessible. The second intrusion, named the Porthmeor granite by Stone and Exley (1984), is exposed about 100 m north of the contact of the main pluton. It forms a small boss with sharp angular corners and is exposed over about 20 m in a N–S direction. The intrusion is composed of sparsely porphyritic Li-siderophyllite granite. Beneath the horizontal upper contact, a layered zone up to 3 m in thickness is developed (Fig. 3a). The upper part of the layered zone consists of pegmatitic granite with unidirectional solidification textures (USTs) alternating with fine- to medium-grained tourmaline granite. In the lower part, the Li-siderophyllite granite is sparsely porphyritic with mica-rich layers. Three temporally, mineralogically and spatially separate dyke generations were distinguished by Stone and Exley

(1984) (Fig. 2). The oldest dyke generation (sample CW67) shows no clear spatial, textural or mineralogical relationship to the pluton and is composed of zinnwaldite–albite granite, being the only known albite granite in the Land's End pluton (Fig. 3b). The younger dyke of sparsely porphyritic Li-siderophyllite (CW66) arises directly from the small intrusion and offsets the albite microgranite (Fig. 3b). The youngest dyke generation is formed of fine-grained tourmaline granite (CW71). Sub-horizontal sections of this dyke show enrichment of tourmaline in the upper part, indicating the fractionation of boron. Like dyke I, dyke III shows no relationship to the exposed granite cupola.

At *Porth Ledden and Priest's Cove* there is evidence for a number of magma batches emplaced in sheets sub-parallel to the shallowly dipping contacts ($<35°$) between the Land's End pluton and the host Mylor Slate Formation (Fig. 2). Based on descriptions by Charoy (1979) and Halls et al. (2002), the following chronological sequence of intrusion has been established:

(1) Fine-grained porphyritic biotite granite (FGG), which occurs only as round enclaves up to 50 cm in diameter in unit (2).

Table 1
Mineralogical compositions and petrographic features of the main granite units of the Land's End pluton

Major granite units	Macroscopic features	Rock-forming minerals	Major accessories (dominant minerals in italics)
Fine-grained porphyritic granite (FGG)	Common kfs megacrysts (>3 cm), sparse crd (up to 1 cm), grey	qz, kfs, pl ($An_{10–33}$), magnesian siderophyllite, crd, ferroan polylithionite	*ap*, *zir*, *mon*, *tur*, xenotime, rutile, ilmenite
Medium- to coarse-grained porphyritic granite (CGG)	Common kfs megacrysts (>3 cm), sparse crd (up to 1 cm), whitish grey	qz, kfs, pl ($An_{10–33}$), magnesian siderophyllite, crd, ferroan polylithionite	*ap*, *zir*, *mon*, *tur*, xenotime, rutile, ilmenite
Albite microgranite	Fine-grained equigranular, white	qz, pl ($An_{7–12}$), ferroan polylithionite, kfs,	*ap*, *zir*, *mon*, *tur*, *ilmenite*, rutile, thorite
Porphyritic Li-siderophyllite granite	Fine-grained with sparse kfs phenocrysts (<3 cm), sparse crd (up to 0.5 cm), whitish grey	qz, kfs, pl ($An_{8–14}$), lithian siderophyllite, crd, siderophyllite	*ap*, *zir*, *mon*, *tur*, xenotime, rutile, ilmenite, thorite, ferrocolumbite, sulphides (chalcopyrite, arsenopyrite, galena), bismuth
Equigranular Li-siderophyllite granite	Fine- to medium-grained equigranular, yellowish white	qz, kfs, tur, pl ($An_{8–14}$), lithian siderophyllite	*ap*, *zir*, *mon*, *rutile*, *ab*, xenotime, thorite, ferrocolumbite, fluorite
Tourmaline granite (Porth Ledden)	fine-grained equigranular, pink	qz, tur, kfs, lithian muscovite, ferroan polylithionite, pl (An_2)	*ap*, *zir*, mon, niobian and tantalian rutile, cassiterite, thorite

The nomenclature of micas by Tischendorf et al. (2001) is applied.

ap—apatite, crd—cordierite, kfs—K-feldspar, mon—monazite, mu—muscovite, pl—plagioclase, qz—quartz, tur—tourmaline, zir—zircon.
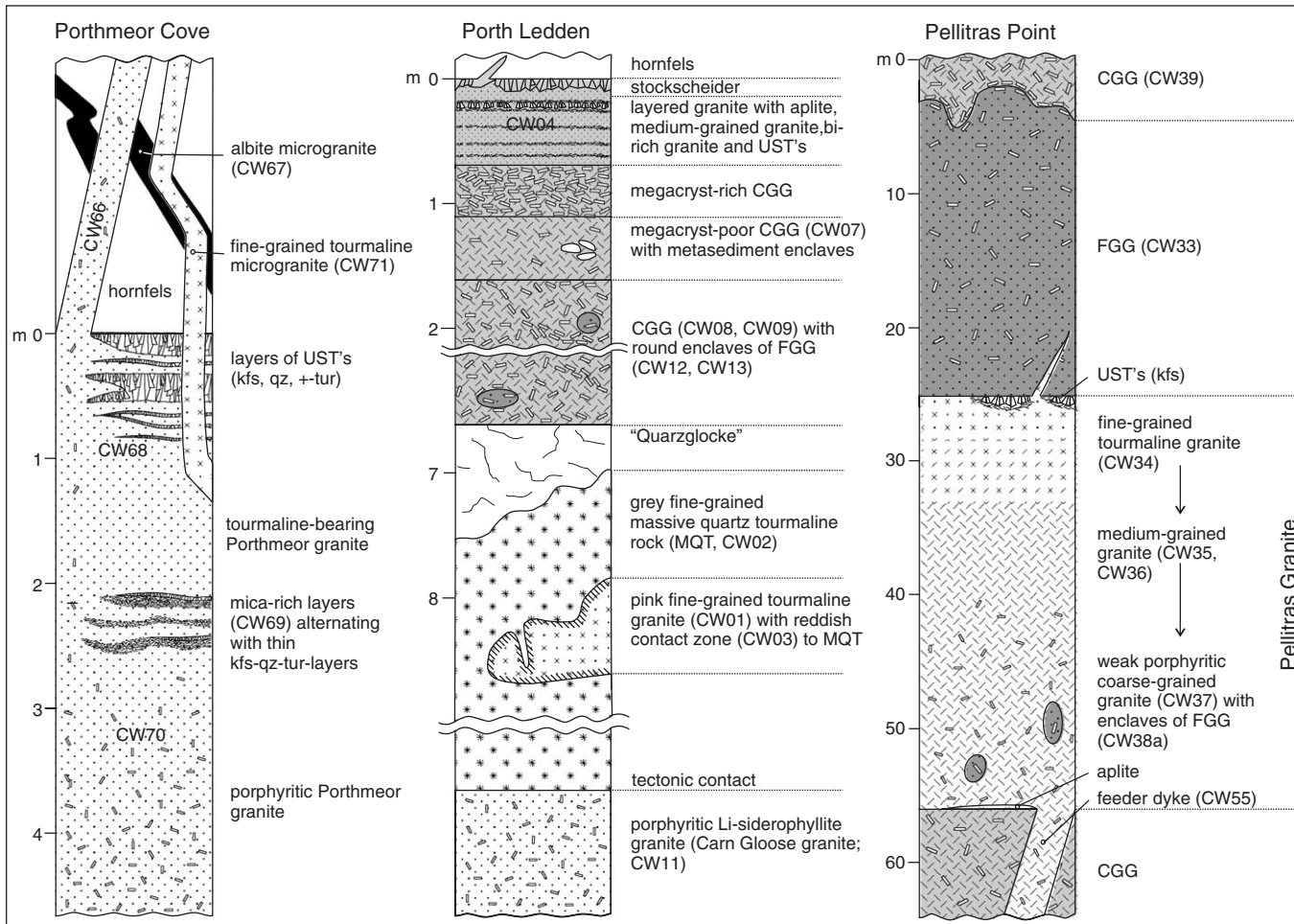
Fig. 2. Schematic vertical cross sections of the Land's End pluton at Porthmeor Cove (Porthmeor granite), Porth Ledden and Pellitras Point with locations of samples in parentheses (CW#). USTs—unidirectional solidification textures.
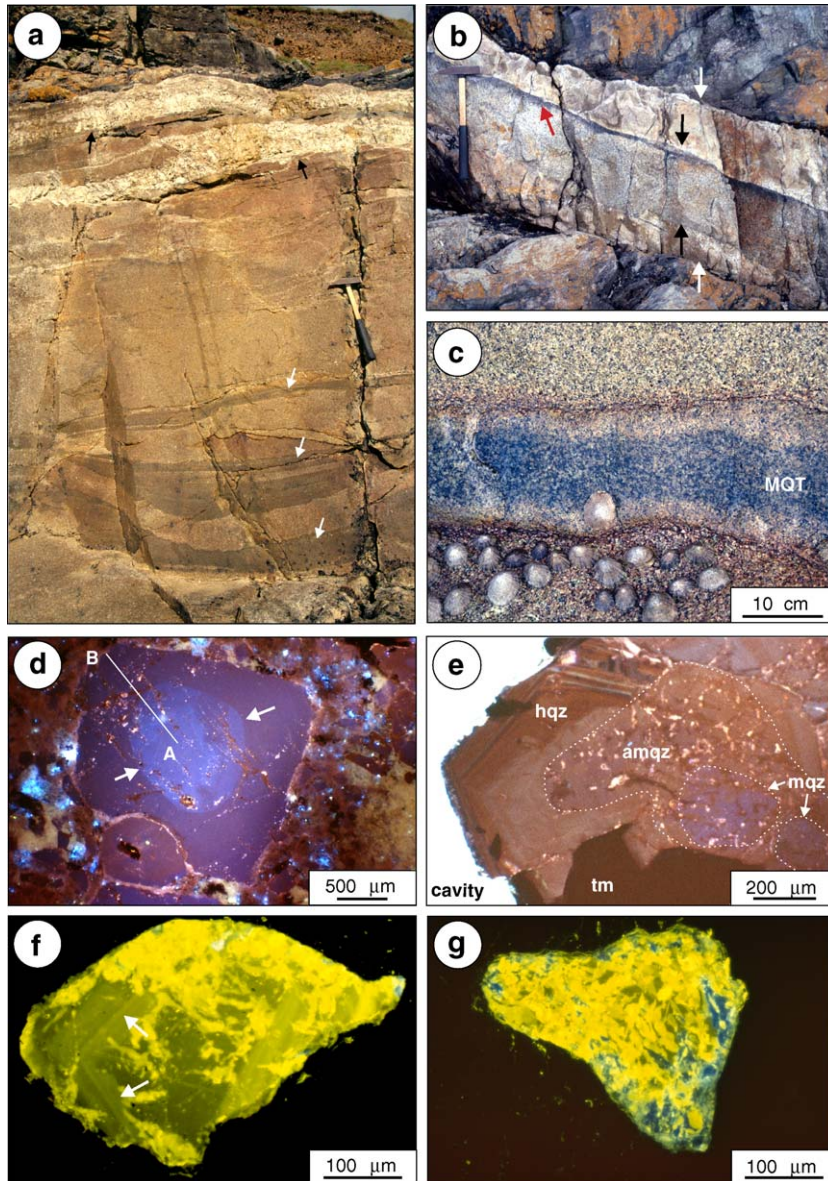
Fig. 3. (a) Layered zone below the upper horizontal contact of the Porthmeor granite at Porthmeor Cove. The layered zone consists of pegmatitic unidirectionally crystalline textures (black arrows) alternating with fine-grained tourmaline-bearing Li-siderophyllite granite. In the lower part, mica-rich layers are developed (white arrows). (b) Older albite microgranite (white arrows) intruded by a tourmaline granite dyke (black arrows). The fractionation of boron led to the enrichment of tourmaline in the upper part of the tourmaline granite dyke (red arrow). (c) Apophysis of massive quartz-tourmaline rock (MQT) within the pink tourmaline granite (here yellowish due to weathering). A silica-rich, 2 to 4 cm wide contact zone is developed along the contact (CW03). (d) CL image of a euhedral zoned quartz phenocryst from the porphyritic Li-siderophyllite granite. The crystal has a rounded blue luminescing core overgrown by violet to red-brown luminescing quartz. (e) CL image showing the textural relationship of quartz (mqz, amqz and hqz) and tourmaline (tm) in the MQT from Porth Ledden. The magmatic quartz (mqz) shows a bluish CL, which is only partly preserved. It contains a number of healed cracks (dark red brown) and bright luminescing inclusions. Partially, the blue CL has changed into red brown CL (amqz—altered magmatic quartz) probably due to diffusion of defects and/or impurities. The magmatic quartz is overgrown by zoned hydrothermal quartz (hqz) which is almost free of healed cracks. (f) CL image of apatite from the pink tourmaline granite (CW01). The unaltered apatite (greyish yellow) shows euhedral oscillatory zones (white arrows). Altered apatite has bright yellow CL. (g) CL image of a completely altered apatite from the MQT (CW02).

(2) Medium- to coarse-grained porphyritic biotite granite (CGG) composing the main sequence. Biotite-rich and aplitic varieties, locally with unidirectional solidification textures (USTs), form a layered sequence of up to 2 m thickness along contacts with the Mylor Slate Formation. The CGG forms the outer carapace and most of the inner parts of the Land's End pluton.

(3) Pink equigranular Li-mica-tourmaline granite follows the main sequence (Fig. 3c). A boundary layer of massive quartz tourmaline rock up to 1 m thick follows the contact with the older CGG. A fine-grained massive quartz–tourmaline rock (MQT; "tourmalinite") occurs in apical irregularities along the inner contact of the Li-mica-tourmaline granite (Fig. 3c; Halls et al., 2002).

(4) Sparsely porphyritic Li-siderophyllite granite is the youngest intrusive unit, containing K-feldspar phenocrysts of an average length <3 cm and sparse, euhedral cordierites up to 1 cm in size. This is the Carn Gloose granite named by Salmon and Shail (1999). The coeval equigranular Li-siderophyllite granites (the St Just wedge granite of Salmon and Shail, 1999) form small irregular patches within the porphyritic Li-siderophyllite granite between Priest's Cove and Porth Nanven. The equigranular Li-siderophyllite granite locally shows miarolitic textures, indicating that magmatic volatiles were concentrated along the contacts (Candela and Blevin, 1995). Thus, the equigranular Li-siderophyllite granite is interpreted as a volatile-enriched variety of porphyritic Li-siderophyllite granite. This explains the interfingering of both varieties and the continuous transitions and nebulous contacts between them, as described by Powell et al. (1999).

The intrusive sequence observed on a small scale in the exposures at Porth Ledden is consistent with the intrusive succession in the inner part of the Land's End Granite as observed at *Pellitras Point and Porth Loe*, but here the units are of significantly larger dimensions. The top unit at Pellitras Point is a porphyritic coarse-grained biotite granite (CGG), which completely encloses a mega-enclave of tabular shape about 300 m in length consisting of porphyritic fine-grained biotite granite (FGG). The FGG mega-enclave represents the first magmatic stage. Contacts with the slightly younger coarse-grained porphyritic biotite granite are rheomorphic and smoothly lobate. Fig. 4a shows a section of the SE contact between the FGG mega-enclave and the CGG. K-feldspar megacrysts of the FGG and CGG are aligned in magmatic flow structures and, locally, megacrysts of the CGG and FGG are aligned parallel to the contacts of the FGG enclave. Both granite varieties contain euhedral cordierites up to 1 cm in size. Metasedimentary enclaves up to 10 cm in size are common in the FGG. A sub-horizontal sheet of equigranular to weakly porphyritic biotite granite up to 30 m thick was emplaced at the lower contact of the FGG mega-enclave (Fig. 4a). This has been named the Pellitras granite by Salmon (1994). From the top to the bottom of the sheet-like intrusion, the Pellitras granite shows an increase in the content of phenocrysts and enclaves, which can be as large as 2 m in diameter; the average crystal size and the content of tourmaline also decreases (Fig. 2). The channel feeding the intrusion of the Pellitras granite is exposed at Porth Ledden, where it forms a steeply dipping dyke ca. 5 m wide.

In summary, three main stages of intrusion can be distinguished. In order of age from older to younger these are:

(1) fine-grained biotite (Mg-siderophyllite) granites (FGG) containing K-feldspar megacrysts with an average length >3 cm

(2) coarse-grained biotite (Mg-siderophyllite) granite (CGG) containing K-feldspar megacrysts with an average length >3 cm

(3) fine-grained porphyritic Li-siderophyllite granites containing sparse K-feldspar megacrysts with an average length <3 cm and co-existing medium-grained equigranular Li-siderophyllite granites.

Differentiates and minor intrusions of tourmaline granite and MQT are spatially and temporally related to the CGG and Li-siderophyllite granites. The affiliation of the zinnwaldite–albite microgranite of Porthmoer Cove to the main intrusion stages of the Land's End pluton remains unclear, but the microgranite is older than the Li-siderophyllite granites. Topaz-bear-
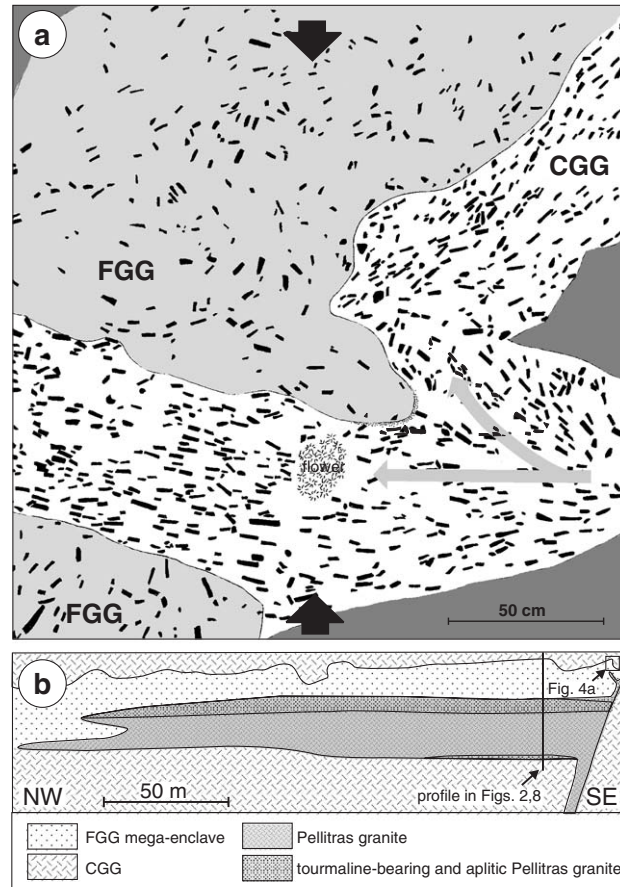
Fig. 4. (a) Alignment of K-feldspar megacrysts (black) along the intra-pluton contact between the FGG and CGG. Grey arrows give the relative flow direction of magma and black arrows indicate the direction of the principle stress (1σ) governing the magmatic flow pattern. The outcrop location is shown in b. (b) Simplified schematic cross-section along the cliffs at Pellitras Point (North of Porth Loe) showing the sheet-like Pellitras granite intrusion emplaced along the subhorizontal contact between the FGG mega-enclave and the CGG.

ing granites, which are known from other parts of the Cornubian Batholith, have not been observed in the Land's End area of Cornwall (e.g., Collins and Coon, 1914).

3. Whole-rock geochemistry

Generally, the granites of the Land's End pluton are strongly peraluminous (A/CNK = 1.1 to 1.4) high-K, calc-alkaline rocks with low phosphorus content (<0.4 wt.%; Fig. 5). The generally high degree of differentiation of the Land's End granites is demonstrated by high contents of Rb, Cs and Nb (Table 2; Fig. 6).

The older FGG have the lowest average SiO_2 contents (66 to 73 wt.%) of the Land's End Pluton and relatively high contents of Ti, Fe, Mg and Ca. The highest Zr/Hf ratio (35 to 41) and the highest ΣREE content (up to 437 ppm) were also found in the FGG. The FGG enclaves from Porth Ledden have slightly higher concentrations of Ti, Fe, Mg, Ca, Zr and REE than the FGG at Pellitras Point and Porth Loe in the southern part of the pluton. Also F, P_2O_5, Th, HREE and HFSE (Zr, Hf, Th, U) are more abundant in the FGG from Porth Ledden. The europium anomaly is more developed in the Porth Ledden FGG (Eu/Eu* = 0.18 to 0.21) than in the FGG at Pellitras Point and Porth Loe (Eu/Eu* = 0.29 to 0.38) (Fig. 7).
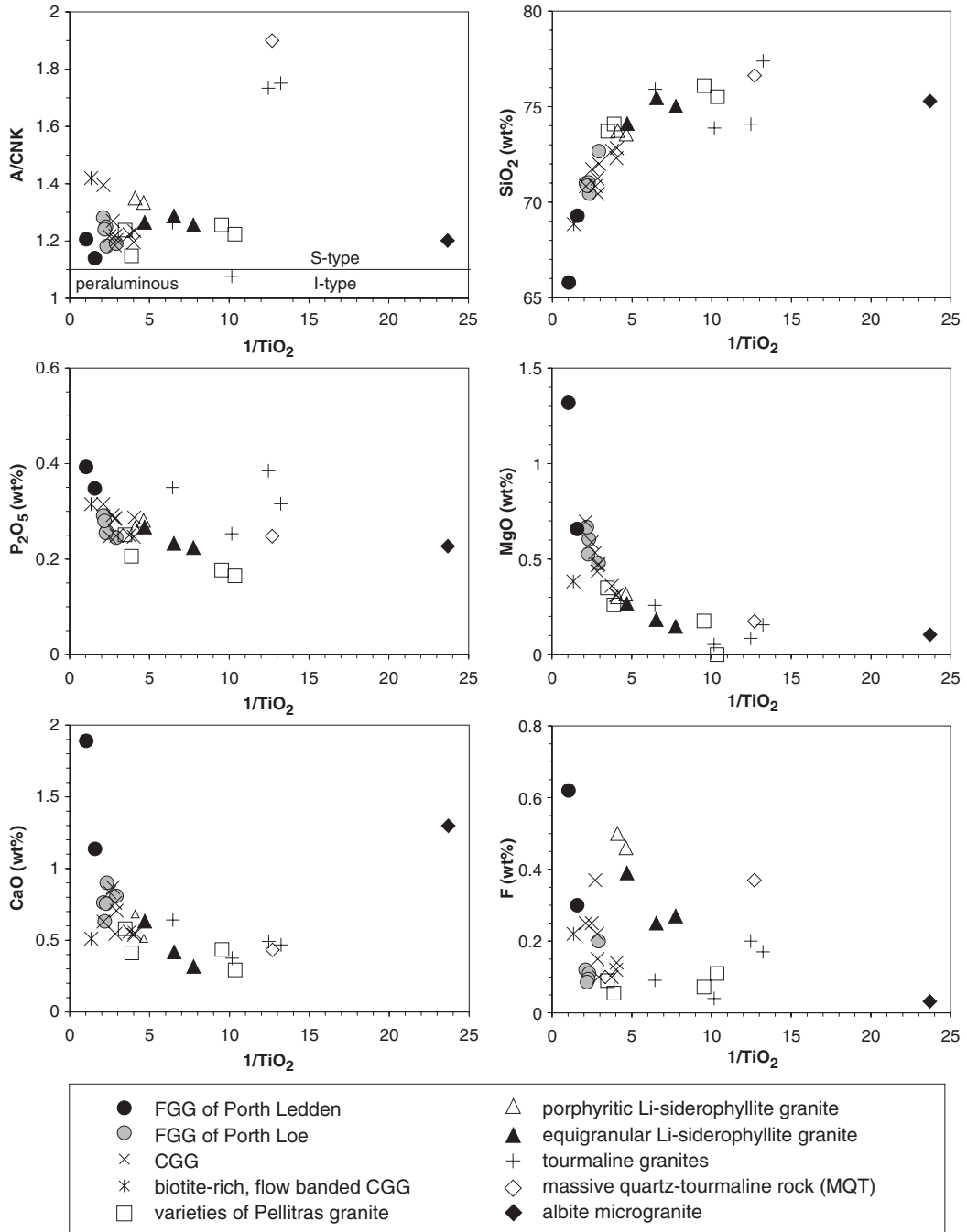
Fig. 5. Variation diagrams, using $1/TiO_2$ as a differentiation index, for selected major and trace element components of the major intrusion phases of the Land's End pluton.

Table 2
Chemical constitution of characteristic samples of the main granite units of the Land's End pluton

Unit	FGG	FGG	CGG	Flow banded CGG	Albite micro-granite	Porphyritic Pellitras granite	Pellitras tourma-line granite	Porph. Li-sidero. granite	Equigr. Li-sidero. granite	Tourmaline-rich Porthmeor granite	Tourmaline micro-granite	Pink tourmaline granite	Contact tourmaline granite/ MQT	MQT
Sample	CW12	CW25	CW20	CW04	CW67	CW37	CW34	CW44	CW32	CW68	CW71	CW01	CW03	CW02
Locality	Porth Ledden	Porth Loe	Porth Curno	Porth Ledden	Porthmeor Cove	Pellitras Point	Pellitras Point	Priest's Cove	Porth Nanven	Porthmeor Cove	Porthmeor Cove	Porth Ledden	Porth Ledden	Porth Ledden
Major elements (wt.%)														
SiO_2	65.79	72.67	71.24	68.85	75.29	73.71	75.52	73.74	75.46	73.88	75.91	74.08	77.39	76.63
Al_2O_3	15.50	14.00	14.77	16.45	14.84	13.94	13.42	13.94	13.45	14.07	13.98	14.22	12.1	13.43
TiO_2	0.97	0.34	0.35	0.74	0.04	0.29	0.10	0.24	0.15	0.10	0.16	0.08	0.08	0.08
Fe_2O_3	1.60	0.56	0.57	1.82	0.59	1.03	0.97	0.84	0.94	0.36	1.49	2.72	2.71	6.26
FeO	3.84	1.59	1.66	1.45	0.43	0.79	0.36	1.3	0.65	0.36	0.36	0.58	0.5	0.65
MnO	0.08	0.03	0.04	0.04	0.02	0.03	0.01	0.03	0.02	0.01	0.02	0.03	0.02	0.05
MgO	1.32	0.48	0.44	0.38	0.10	0.35	<0.05	0.30	0.18	0.05	0.26	0.08	0.16	0.17
CaO	1.89	0.81	0.76	0.51	1.30	0.58	0.29	0.68	0.42	0.38	0.64	0.49	0.47	0.43
Na_2O	3.45	2.80	2.77	3.47	5.45	2.55	2.50	2.44	2.62	2.85	5.75	0.56	0.43	0.70
K_2O	3.46	5.24	6.03	4.58	0.95	5.55	5.84	4.69	4.96	7.10	0.40	5.89	4.94	0.14
P_2O_5	0.39	0.24	0.28	0.32	0.23	0.25	0.16	0.26	0.23	0.25	0.35	0.38	0.32	0.25
LOI	1.18	0.98	0.86	1.17	0.61	0.77	0.80	1.28	0.81	0.57	0.55	0.63	0.69	0.81
F	0.62	0.20	0.22	0.22	0.03	0.09	0.11	0.50	0.25	0.04	0.09	0.20	0.17	0.37
Cl	0.05	0.04	0.05	0.03	0.01	0.04	0.01	0.04	0.02	0.03	0.01	0.01	0.02	0.02
B	<0.001	0.005	0.004	>0.1	0.020	0.050	0.060	0.020	>0.1	0.010	>0.1	>0.1	>0.1	>0.1
S	0.013	0.022	0.016	0.024	0.005	0.029	0.075	0.043	0.014	0.005	0.019	0.008	0.008	0.006
O=(F,Cl,B,S)	0.280	0.109	0.114	0.092	0.033	0.098	0.131	0.256	0.191	0.034	0.123	0.165	0.154	0.236
Sum	99.9	99.9	99.9	100.0	99.9	99.9	100.1	100.1	100.0	100.0	100.0	99.9	99.9	99.8
Trace elements (ppm)														
Ga	40	30	30	80	20	30	30	25	30	20	25	40	40	40
Zn	80	50	40	40	30	40	40	60	30	30	30	50	40	60
Rb	547	412	460	564	94	436	520	731	592	434	13	505	322	2
Sr	73	90	85	29	139	73	15	18	18	51	52	24	33	7
Y	31.2	17.2	19.3	74.8	7.1	16.0	11.1	17.9	14.7	12.0	8.5	9.8	12.9	6.8
Zr	378	138	180	308	40	120	36	101	66	51	38	38	39	38
Nb	26	21	23	71	27	21	21	31	23	27	11	29	37	24
Sn	5	15	12	20	20	12	100	30	15	10	25	10	25	5
Cs	27.0	25.0	37.7	28.3	10.3	20.6	23.7	53.8	29.9	12.9	1.8	13.4	11.1	1.3

Ba	186	176	270	56	48	166	17	40	26	96	7	126	388	2
La	84.3	26.1	42.3	35.0	5.8	20.0	7.1	20.3	12.3	9.7	5.8	3.7	5.0	2.3
Ce	195.4	63.2	98.4	89.9	10.8	47.4	16.9	47.7	29.6	18.6	12.6	9.3	12.6	5.9
Pr	23.5	7.6	11.9	11.3	1.4	5.9	2.1	5.8	3.6	2.6	1.8	1.2	1.7	0.8
Nd	91.1	28.5	44.3	43.1	4.9	22.0	7.6	21.9	13.7	9.9	7.7	4.6	6.6	3.1
Sm	16.0	5.9	8.8	10.4	1.1	4.9	1.8	4.7	3.2	2.4	2.0	1.3	2.1	1.0
Eu	0.77	0.59	0.81	0.30	0.50	0.46	0.08	0.20	0.13	0.28	0.28	0.13	0.25	0.10
Gd	10.40	4.46	6.01	9.49	1.02	3.87	1.58	3.66	2.65	2.06	1.70	1.36	1.96	0.89
Tb	1.33	0.66	0.81	1.84	0.19	0.59	0.31	0.59	0.46	0.37	0.27	0.27	0.38	0.18
Dy	6.66	3.76	4.16	12.20	1.20	3.28	1.93	3.39	2.72	2.17	1.63	1.73	2.53	1.21
Ho	1.14	0.65	0.69	2.42	0.23	0.55	0.35	0.61	0.52	0.40	0.30	0.31	0.47	0.23
Er	3.05	1.78	1.83	8.03	0.75	1.56	1.18	1.76	1.52	1.18	0.90	0.98	1.46	0.69
Tm	0.40	0.24	0.23	1.29	0.11	0.23	0.20	0.27	0.24	0.18	0.14	0.17	0.24	0.12
Yb	2.53	1.54	1.54	9.27	0.88	1.47	1.42	1.78	1.65	1.28	0.91	1.22	1.88	0.91
Lu	0.36	0.23	0.20	1.28	0.12	0.22	0.21	0.24	0.22	0.17	0.13	0.17	0.25	0.12
Hf	9.14	3.97	4.87	9.55	2.05	3.53	1.51	3.18	2.27	2.19	1.54	1.53	1.64	1.62
Ta	1.94	2.75	2.94	12.15	12.60	4.13	4.33	6.50	5.97	7.50	3.41	8.78	9.94	8.26
Pb	15.4	22.9	24.5	24.7	14.8	15.2	13.2	5.2	10.6	30.8	1.9	6.6	8.3	2.7
Th	43.4	21.2	28.1	46.2	4.4	15.7	6.9	16.9	11.2	6.9	5.8	4.0	4.3	3.3
U	10.6	11.0	12.8	38.0	6.4	5.3	5.5	33.0	8.1	5.0	4.1	3.1	7.1	4.1
Be	5	2	10	3	5	5	2	8	2	2	5	3	3	5
Cr	31	29	29	22	23	48	25	<20	53	21	52	50	34	45
Co	8	2	4	12	3	4	<0.5	5	2	<0.5	<0.5	<0.5	<0.5	<0.5
Cu	15	60	15	15	20	15	120	25	15	20	40	50	20	30
Li	120	60	80	80	40	60	60	100	80	30	25	50	50	60
Ni	15	10	6	6	4	8	4	5	5	<3	5	4	4	3
Sc	12	8	6	8	3	6	5	8	5	4	4	6	5	6
V	60	30	30	12	6	20	8	15	12	8	10	6	6	5
Zr/Hf	41	35	37	32	19	34	24	32	29	23	25	25	24	23
Y/Ho	27.5	26.5	28.1	30.9	30.8	28.9	31.3	29.3	28.5	30.1	28.2	31.4	27.4	29.9
Th/U	4.1	1.9	2.2	1.2	0.7	3.0	1.2	0.5	1.4	1.4	1.4	1.3	0.6	0.8
Eu/Eu*	0.18	0.35	0.34	0.09	1.45	0.32	0.14	0.15	0.13	0.39	0.46	0.29	0.37	0.32
La$_N$/Yb$_N$	23.1	11.7	19.0	2.6	4.5	9.4	3.4	7.9	5.2	5.3	4.4	2.1	1.8	1.8
$\sum$REE	437	145	222	236	29	112	43	113	73	51	36	26	37	18

Eu/Eu*=Eu/v(Sm+Gd).

La$_N$/Yb$_N$=La(chondrite normalised)/Yb(chondrite normalised).

CGG—medium- to coarse-grained porphyritic granite, equigr. Li-sidero. granite—equigranular lithian siderophyllite granite, FGG—fine-grained porphyritic granite, MQT—massive quartz tourmaline rock, porph. Li-sidero. granite—porphyritic lithian siderophyllite granite.
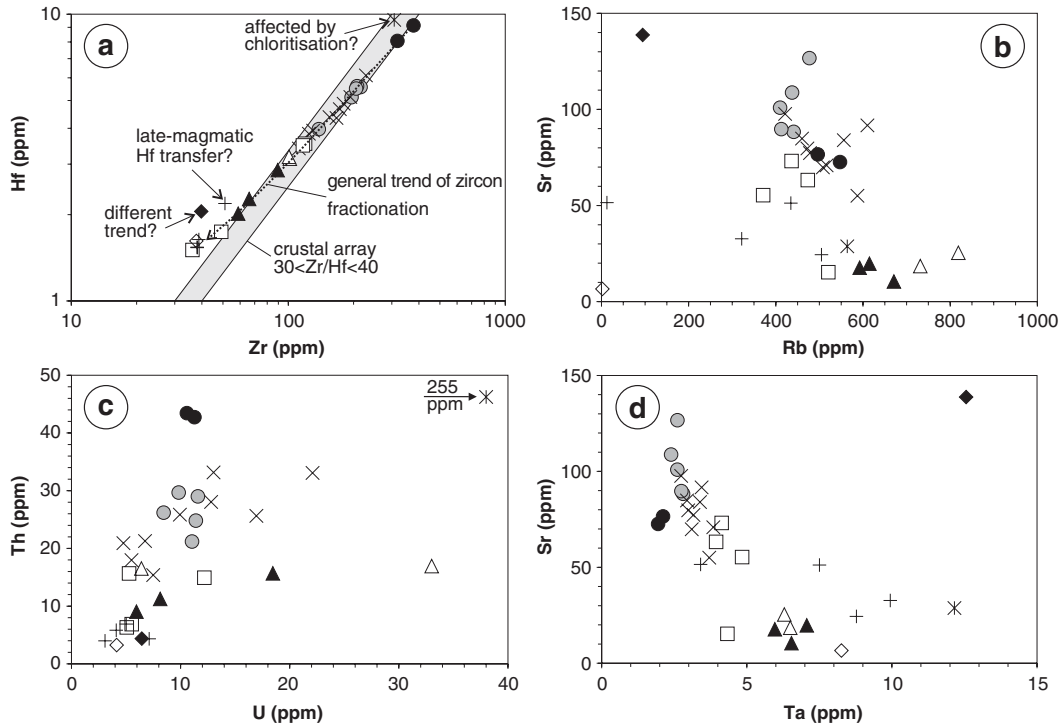
Fig. 6. (a) Log Zr–log Hf diagram (after Raimbault et al., 1995) for the Land's End granites. The general trend reflects the fractionation of zircon in granitic melts. For further explanation see text. (b–d) Trace element variation plots for characteristic samples of the Land's End pluton. See Fig. 5 for symbols.

The CGG of the southwestern margin of the Land's End pluton shows a relatively homogenous composition with SiO_2 contents between 70 and 73 wt.%. The CGG contains slightly lower concentrations of Sr, HFSE and REE in comparison to the FGG. The high Zr/Hf ratio (32 to 38) is characteristic of crustal materials. The biotite-rich flow-banded CGG (CW04) shows a much stronger negative europium anomaly (Eu/Eu*=0.09) and, by comparison with the average CGG, it is enriched in HREE. The biotite from this sample and sample CW27 is mostly chloritised. The process of chloritisation may be responsible for the introduction of heavy REE into the system (Alderton et al., 1980). The HREE enrichment in the CGG of Porth Ledden (CW04) and central Sennen Cove (CW27) is explained by the higher contents of apatite and zircon in these rocks. In both biotite-rich samples, the depletion in LREE and the enrichment of HREE is attributed to chloritisation (Alderton et al., 1980).

The Pellitras granite, which is interpreted as a slightly more differentiated batch of the CGG,

shows strong vertical fractionation internally and has a correspondingly wide variation in composition. Two main facies can be distinguished. A sparsely porphyritic Mg-siderophyllite granite forms the lower 20 m of the sheet, and the tourmaline-bearing varieties make up the upper 10 m (Fig. 8). The spider diagram in Fig. 8 shows the minor and trace element variation of the Pelltiras granites normalised with respect to the most primitive Land's End granite (FGG—sample CW12). The composition of the Mg-siderophyllite granite is similar to that of the CGG, but with slightly lower concentrations of total FeO, MgO, CaO, Sr, Ba, HFSE and LREE. The tourmaline-bearing Pellitras granite is richer in Cu, Sn and B than other facies of the Pellitras granite and the contents of tFeO, MgO, CaO, Sr, Ba, HFSE and LREE are distinctly lower. Fig. 8 illustrates that Sn and Cu enrichment of the boron-rich melt portions had already begun during the main stage of the evolution of the Land's End pluton.

The chemistry of the albite microgranite from Porthmeor Cove is described here for the first time.
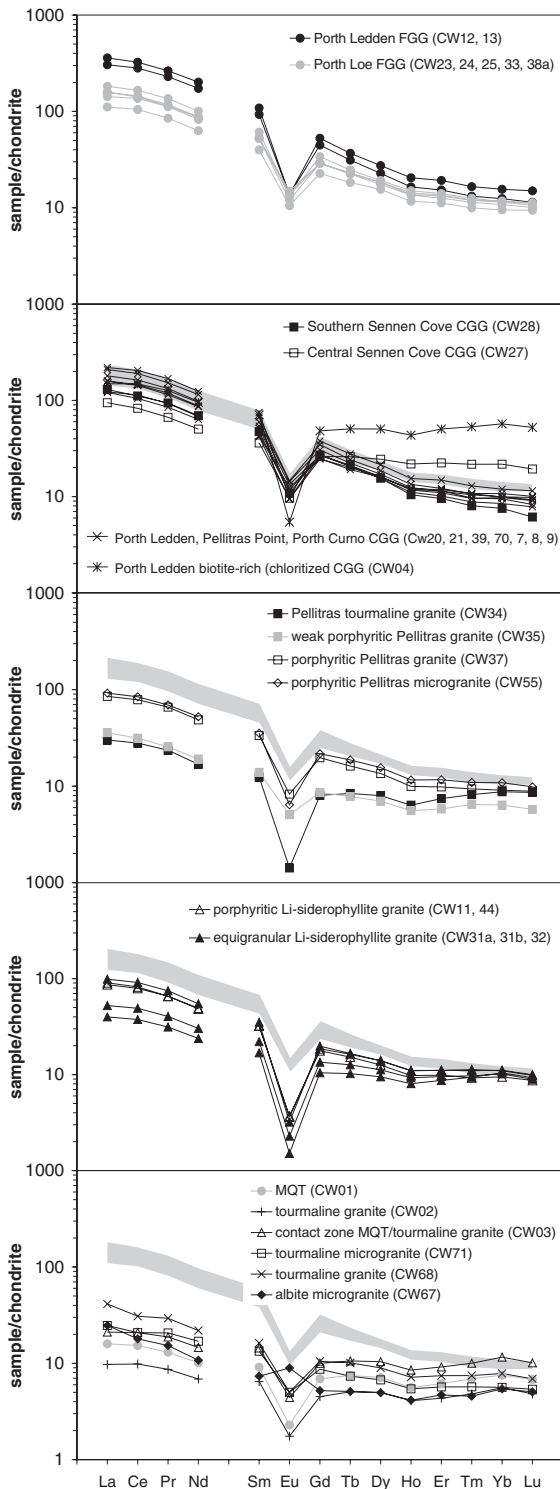
It is the only known occurrence of this type of granite in the Land's End pluton. It has a chemical signature quite distinct from the other granites of the Land's End pluton. Despite the high SiO_2 content of about 75 wt.%, the granite is rich in CaO (1.3 wt.%) and Na_2O (5.45 wt.%) but has low abundances of K_2O, TiO_2, MgO, tFeO, F, Zr and Ba. It is the only unit of the Land's End pluton showing a positive europium anomaly (Eu/Eu*=1.45) which indicates local evolution of a separate albite-rich melt probably from a separate magmatic source.

The SiO_2-rich (73 to 76 wt.%) Li-siderophyllite granites have high Rb, B and Ta and low Ca, Ti, Mg, Ba, Zr and Th and very low Sr as compared with the CGG and FGG. The granites show elevated F concentrations between 0.25 and 0.5 wt.%, but the rocks are free of topaz. The strong europium anomaly (Eu/Eu*=0.11 to 0.15) suggests marked fractionation of feldspar. The porphyritic Li-siderophyllite granite has slightly higher concentrations of TiO_2, MgO and CaO than the more evolved B-rich equigranular Li-siderophyllite granites.

The tourmaline granites at Porth Ledden and Pellitras show the highest degree of differentiation within the Land's End intrusive sequence. Generally, they are characterised by the enrichment of tFeO, P_2O_5 and Ta and by depletion of Na_2O, K_2O, Th and U. The tourmaline microgranite from Porthmeor Cove (CW71; Fig. 2) has a distinct geochemical signature which cannot be related to any of the granites exposed there. The microgranite contains much less K_2O, has a high Na_2O content and is extremely rich in Fe_2O_3 (6.26 wt.%). The SiO_2-rich (76.6 wt.%) MQT of Porth Ledden has very low K_2O (0.14 wt.%) and ΣREE (18 ppm) and it has effectively no Rb, Sr, Ba and Cs due to the absence of feldspar.

In the sequence from the FGG, CGG towards the Li-siderophyllite granites and tourmaline granites, the Zr/Hf ratio shows a progressive almost linear decrease (Fig. 6). The trend is due to the fractionation of zircon (e.g., Linnen and Keppler, 2002) and a relative enrichment of Hf (Fig. 8) because Hf has a higher affinity with the peraluminous melts than Zr (Linnen, 1998). Three

Fig. 7. Chondrite-normalised REE pattern for the main intrusive phases of the Land's End pluton. The grey pattern in the background corresponds to the REE pattern of the Porth Loe FGG shown in the upper diagram.
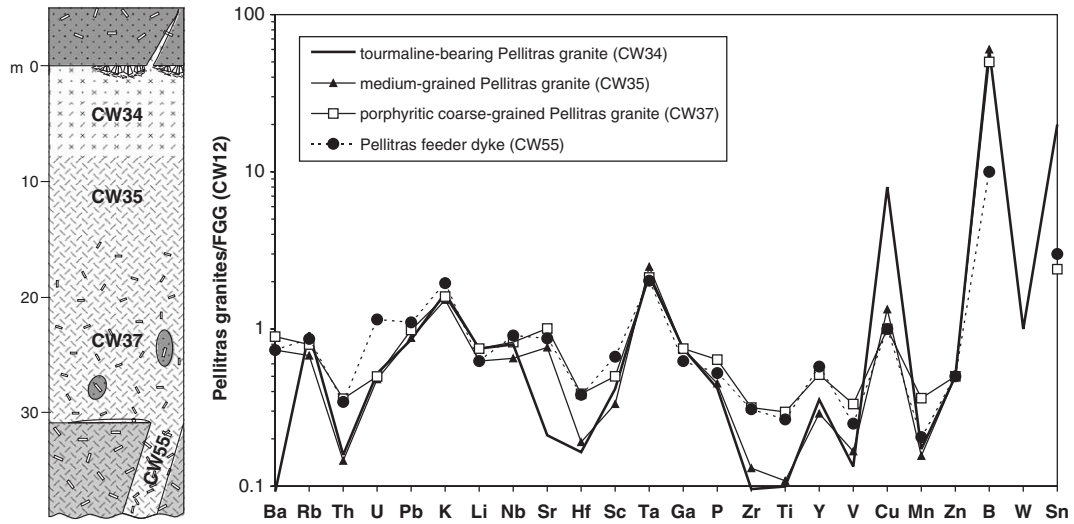
Fig. 8. Spider diagram of minor and trace element variation compared with the most primitive Land's End granite (FGG—sample CW12) along a vertical profile across the sheet-like Pellitras granite. The column in the left illustrates the sample location within the profile.

samples do not conform to this general trend. In the banded CGG and in the tourmaline granite of Pellitras, the higher Hf may be due to late-magmatic or hydrothermal transfer of Hf. In the case of the banded CGG, this is associated with the process of chloritisation (Raimbault et al., 1995). The low Zr/Hf ratio (19) in the albite microgranite is probably caused by a difference in the trend of zircon fractionation.

3.1. Rb–Sr and Sm–Nd isotope ratios of whole rocks

All initial isotope ratios reported here were calculated assuming a 280 Ma age for the intrusion. (Darbyshire and Shepherd, 1985; Chesley et al., 1993). Two whole-rock samples, one from the Li-siderophyllite granite (CW44), and one from the pink tourmaline granite (CW01) yield unrealistically low initial $^{87}Sr/^{86}Sr$ ratios (0.673 and 0.699, Table 3). It is well

known that in evolved granitic or volcanic rocks the addition of Rb or loss of radiogenic ^{87}Sr can produce anomalous Sr ratios, which are far too low to be of geological significance (e.g., Schleicher et al., 1983; Gerstenberger, 1989). Charoy (1986) undertook a Rb–Sr study of the Carnmenellis pluton and proposed post-magmatic influx of Rb into the granite. Pertubation of the Rb–Sr system is particularly common in evolved rocks with high Rb/Sr ratios and, in general, reliable initial Sr isotope ratios can only be expected from low Rb/Sr samples. The Li-siderophyllite granite and the pink tourmaline granite samples yield exceptionally high $^{87}Rb/^{86}Sr$ ratios of 119 and 61 (Table 3) Therefore, it seems very likely that the isotopic signatures of both rock types did not evolve in a closed system. Both rocks come from nearby localities (Porth Ledden and Priest's Cove) and it seems likely that either this particular zone or the evolved rocks from

Table 3

Rb–Sr and Sm–Nd analytical data for the Land's End granites. For element concentrations see Table 2

Unit (sample)	$^{87}Rb/^{86}Sr$	$^{87}Sr/^{86}Sr$	$^{87}Sr/^{86}Sr_{(T)}$	$^{147}Sm/^{144}Nd$	$^{143}Nd/^{144}Nd$	$\varepsilon_{Nd}(t)$	$\varepsilon_{Nd}(0)$	$T_{DM}*$	$T_{DM}**$
FGG (CW25)	13.36	0.761992	0.70877	0.1248	0.512209	−5.8	−8.4	1.52	1.51
CGG (CW20)	15.79	0.772363	0.70944	0.1206	0.512144	−6.9	−9.6	1.56	1.60
Lithian siderophyllite granite (CW44)	119.25	1.147977	0.67291	0.1317	0.512191	−6.4	−8.7	1.67	1.55
Pink tourmaline granite (CW01)	61.26	0.943363	0.69930	0.1780	0.512289	−6.1	−6.8	3.18	1.54
Albite microgranite (CW67)	1.97	0.720917	0.71307	0.1344	0.512090	−8.5	−10.7	1.91	1.72

$T_{DM}*$ model ages calculated according to DePaolo et al. (1991). $T_{DM}**$ model ages calculated according to Liew and Hofmann (1988). CGG—medium- to coarse-grained porphyritic granite, FGG—fine-grained porphyritic granite.

this zone were affected by autohydrothermal alteration or later fluid exchange. In the other samples from the Land's End pluton, initial isotopic ratios appear to increase from the fine-grained biotite granite (CW25, 0.70877) through the coarse-grained biotite granite (CW20, 0.70944) to the albite microgranite (CW67, 0.71307). In general, the isotopic compositions fit with those reported in the literature for the Cornubian granitoids. Hawkes and Dangerfield (1978) determined $^{87}Sr/^{86}Sr$ ratios of 0.7086 for the St. Austell granite while Darbyshire and Shepherd (1985) obtained values from the Land's End, Carnmenellis, St. Austell, Bodmin and Dartmoor granites that average around 0.7119 with a spread of 0.7095 (St. Austell) to 0.7140 (Bodmin). Hawkes et al. (1975) reported values of 0.7064 to 0.7149 for "elvans".

Samples from the Land's End pluton investigated in our study have non-radiogenic $^{143}Nd/^{144}Nd$ ratios with $\varepsilon_{Nd}(t)$ values ranging from -5.8 to -8.5 (Table 3). For comparison, $\varepsilon_{Nd}(t)$ values obtained by Darbyshire and Shepherd (1994) for the main Cornubian plutons range from -4.7 to -7.1. Within the Land's End pluton, the Li-siderophyllite granite and the pink tourmaline granite have $\varepsilon_{Nd}(t)$ values (-6.4 and -6.1) similar to the fine-grained biotite granite (-5.8) and the coarse-grained biotite granite (-6.9), whereas the albite microgranite has a distinctively lower $\varepsilon_{Nd}(t)$ value of -8.5.

4. Mineralogy

4.1. Alkali feldspar

Mineral textures within the K-feldspar phenocrysts, such as zonal arrangement of plagioclase, quartz, biotite, K-feldspar, apatite and zircon inclusions, are shown in Fig. 9. The composition of biotite inclusions within the phenocryst generally matches that of the biotite in the groundmass of the host rocks as described below. The anorthite component of plagioclase inclusions (An_{20-25}) is similar to the composition of the cores of plagioclase phenocrysts in the host rock. Occasionally, plagioclase-mantled K-feldspar (rapakivi feldspar) occurs in the FGG (Salmon and Powell, 1998) and CGG.

Major and minor elements in the feldspar phenocrysts and groundmass feldspar were determined along traverses using electron probe microanalyses (EPMA). The average composition of megacrysts in the FGG is $Or_{92}Ab_8An_0$ ($n=115$), for the Porth Curno CGG it is same ($n=68$) and for the Porth Ledden CGG it is $Or_{95}Ab_5An_0$ ($n=48$). Because the K-feldspar megacrysts are microperthitic, about 20% of the analyses gave albite compositions. The composition of the albite domains in the microperthitic megacrysts lies in the range $Or_{2-4}Ab_{94-96}An_{1-2}$. The average Ba content of K-feldspar megacrysts (861 to 1212 ppm) is much higher than that in the K-feldspar from the groundmass (177 to 402 ppm). As in the case of Ba, the average Sr content (118 to 150 ppm) of the megacrysts is higher than that of the K-feldspar in the matrix (27 to 76 ppm).

Three profiles from core to rim in K-feldspar megacrysts from different granites of the Land's End pluton were analysed by LA-ICP-MS (43 analyses). Some representative LA-ICP-MS analyses of minor and trace elements are listed in Table 4. There are minor differences in Ba, Rb, Ga, Ta, REE and Pb between K-feldspar megacrysts from the FGG at Porth Loe, the CGG from Porth Ledden and CGG from Porth Curno. However, there is distinct intra-granular variation in Rb and Ba in the megacrysts, particularly in those from the FGG. Generally, Rb increases from core to rim (Figs. 10 and 11) but steps in concentration of up to 330 ppm within distances of 200 μm indicate that the overall progression in the pattern of geochemical evolution in the crystallising magma was intermittently disturbed, probably by magma recharge.

The megacryst from the FGG shows the widest scatter of Ba, Rb and Sr contents, indicative of crystallisation in a more variable environment. The Ba variation from 500 to 1870 ppm shows a positive correlation with REE, Sr and Ga, whereas Rb (726 to 1164 ppm) shows a positive correlation with Pb (31 to 65 ppm), Ta and Ge. Generally, Rb, Pb and Ta increase and Ba, Sr, Ga, Ti and REE in K-feldspar decrease during magmatic evolution (Smith, 1983; Long and Luth, 1986; Neiva, 1995; Larsen, 2002). Ba contents in K-feldspar megacrysts from the CGG's range from 480 to 1070 ppm. The average Ba in the core of megacryst CW08 is 1200 ppm and increases somewhat to 1900 ppm on the rim. Sr is almost constant whereas Rb increases. The generally low content of Ba, Ga, LREE and the abundance of Rb, Pb, Ta, Sn indicate a high degree of differentiation
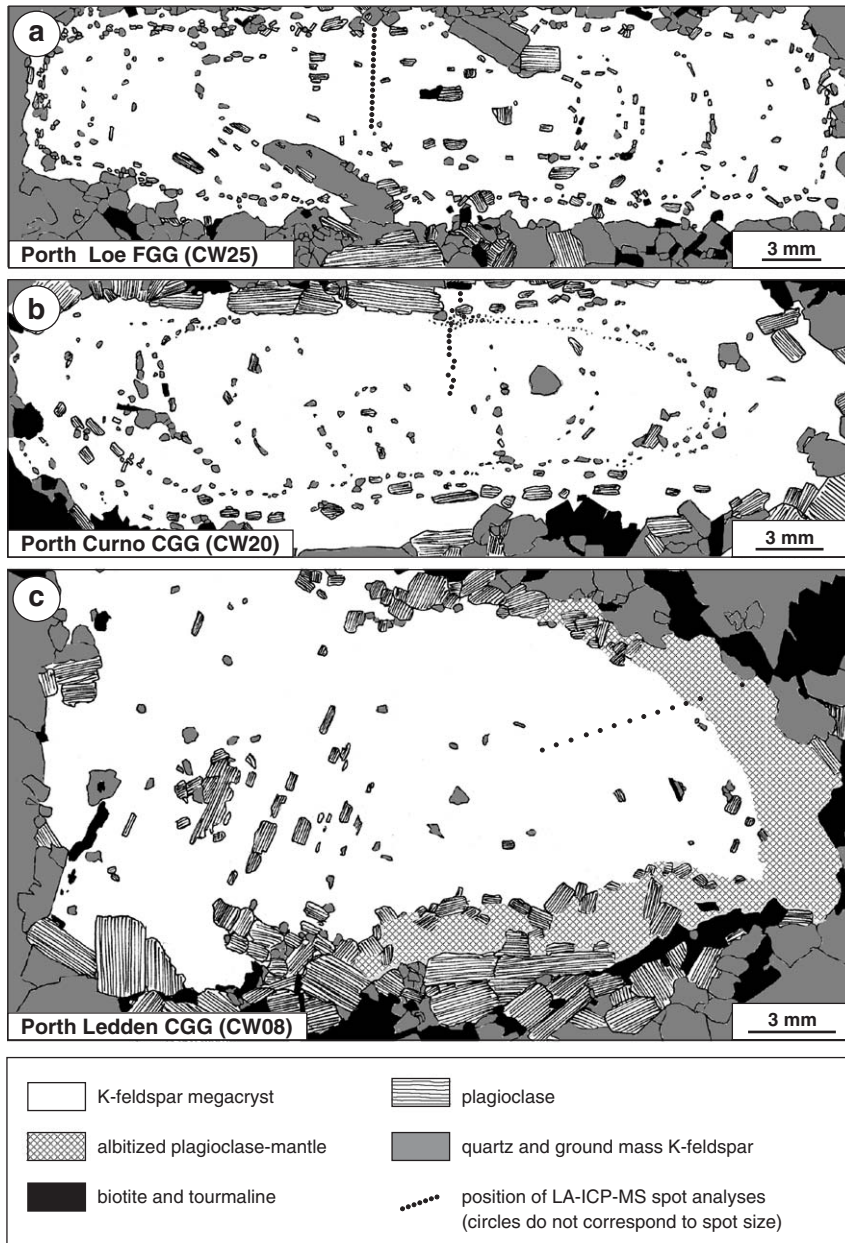
Fig. 9. Drawing of thin section of K-feldspar megacrysts from the (a) FGG of Porth Loe, (b) CGG of Porth Curno and (c) CGG of Porth Ledden, showing locations of ICP-MS profiles.

within the host magma. The Porth Curno CGG megacrysts have a slightly lower average Pb content (45 ppm) than the megacrysts from the other two granites with 60 and 57 ppm Pb, respectively. Because the Pb content from the Porth Curno megacryst plots outside

the general trend, it is concluded that secondary remobilisation caused some loss of Pb from the megacryst (Ludwig and Silver, 1977).

Overall, the shape of the chondrite normalised REE patterns of the three megacrysts is similar, whereas the

Table 4
Representative LA-ICP-MS analyses (ppm) of minor and trace elements in K-feldspar megacrysts from the Land's End pluton

Sample	Limits of detection	FGG (Porth Loe)			CGG (Porth Curno)			CGG (Porth Ledden)		
		CW25	CW25	CW25	CW20	CW20	CW20	CW08	CW08	CW08
	Example	fe24a10	fe24a14	fe24a13	fe25a07	fe25a04	fe25a05	fe25b09	fe25b12	fe25b18
SiO_2 (wt.%)	0.03	63.48	63.1	63.52	63.29	63.27	63.25	63.18	61.92	62.71
Sc	0.6	7.4	7.0	5.4	6.9	7.7	7.1	5.2	4.6	4.8
Ti	1.5	63.1	98.8	122	61	58	45	97.3	86.8	87.5
Mn	0.2	49.7	9.0	10.9	41.8	83.1	105.6	26.8	11.1	9.0
Fe	13	933	586	541	291	442	825	294	156	163
Ga	0.1	44.2	56.22	42	56	56	50	45.5	38.4	36.9
Ge	0.2	2.20	1.60	1.60	1.49	1.60	1.61	1.75	1.17	1.19
Rb	0.1	950	799	877	738	774	726	1164	778	818
Sr	0.1	111	134	174	127	139	103	116	127	120
Y	0.006	0.457	0.290	0.291	0.194	0.158	0.112	0.148	0.053	0.039
Sn	0.2	27.7	18.6	31.9	24.3	22.3	20.4	25.1	26.6	28.7
Ba	0.3	614	1003	648	1070	1023	926	810	688	623
La	0.006	3.917	3.663	2.983	1.896	1.773	0.875	1.975	2.094	2.068
Ce	0.005	6.204	4.236	2.879	1.688	1.920	0.763	1.993	1.823	1.671
Pr	0.002	0.721	0.325	0.200	0.101	0.106	0.043	0.097	0.080	0.094
Nd	0.022	2.594	1.155	0.562	0.241	0.316	0.053	0.264	0.161	0.198
Sm	0.035	0.440	0.157	0.050	0.051	<0.037	<0.035	<0.080	<0.100	<0.062
Eu	0.006	1.347	1.561	1.657	1.404	1.418	1.037	1.343	1.381	1.267
Gd	0.045	0.408	0.165	0.074	0.041	0.070	0.045	<0.156	<0.071	<0.116
Tb	0.006	0.037	0.013	<0.013	<0.006	<0.008	<0.009	<0.013	<0.013	<0.021
Dy	0.013	0.137	0.054	0.031	0.013	<0.013	<0.013	<0.060	<0.036	<0.054
Ho	0.008	0.020	0.012	<0.008	<0.008	<0.010	<0.010	<0.017	<0.013	<0.020
Er	0.011	0.039	0.012	<0.027	<0.013	<0.018	<0.030	0.013	0.011	<0.110
Tm	0.005	<0.008	<0.005	0.009	<0.010	<0.008	<0.007	<0.012	<0.019	<0.015
Yb	0.022	<0.027	<0.022	<0.039	<0.043	<0.022	<0.027	<0.105	<0.063	<0.115
Lu	0.004	<0.009	<0.004	<0.011	<0.009	<0.013	<0.009	<0.011	<0.020	0.004
Hf	0.094	0.062	0.134	<0.096	0.104	0.113	0.074	<0.094	0.106	<0.097
Ta	0.003	0.420	0.694	0.779	0.668	0.644	0.628	0.726	0.696	0.548
Pb	0.1	59.7	61.2	65.1	49.1	50.2	36.8	61.2	53.3	55.1
Bi	0.005	0.048	0.018	0.019	0.031	0.1223	0.0346	0.775	0.014	0.019

Limits of detection were calculated for each analysis separately, so those given are representative examples only.
CGG—medium- to coarse-grained porphyritic granite, FGG—fine-grained porphyritic granite.

concentrations of REE may vary by a factor of 10. The pattern is characterised by a strong positive Eu anomaly and enrichment of La and Ce (Fig. 12). The REE concentration in the FGG megacryst is about 3 to 4 times higher than that in the two CGG megacrysts.

4.2. Plagioclase

Plagioclase from the FGG has an average crystal core composition of $Or_{3.5}Ab_{70.2}An_{26.3}$ ($n=61$), with the margin much closer to albite in composition $Or_{3.2}Ab_{84.0}An_{12.8}$ ($n=11$). Plagioclase from the CGG is similar to that from the FGG, with core compositions

of $An_{23.4}$ ($n=20$) and a marginal growth zone with $An_{11.7}$ ($n=4$). The most calcic plagioclase found in crystal cores in the FGG and CGG has a composition of An_{33}. The Li-siderophyllite granites and the albite microgranite contain albitic plagioclase with an anorthite component ranging from An_8 to An_{14}. Most of the tourmaline granites show similar plagioclase compositions. Only the pink tourmaline granite from Porth Ledden contains nearly pure albite crystals (An_2), which may represent complete replacement of pre-existing K-feldspar under sub-solidus conditions (e.g., Lee and Parsons, 1997). The rims of plagioclase from the FGG and CGG, and the plagioclase from the
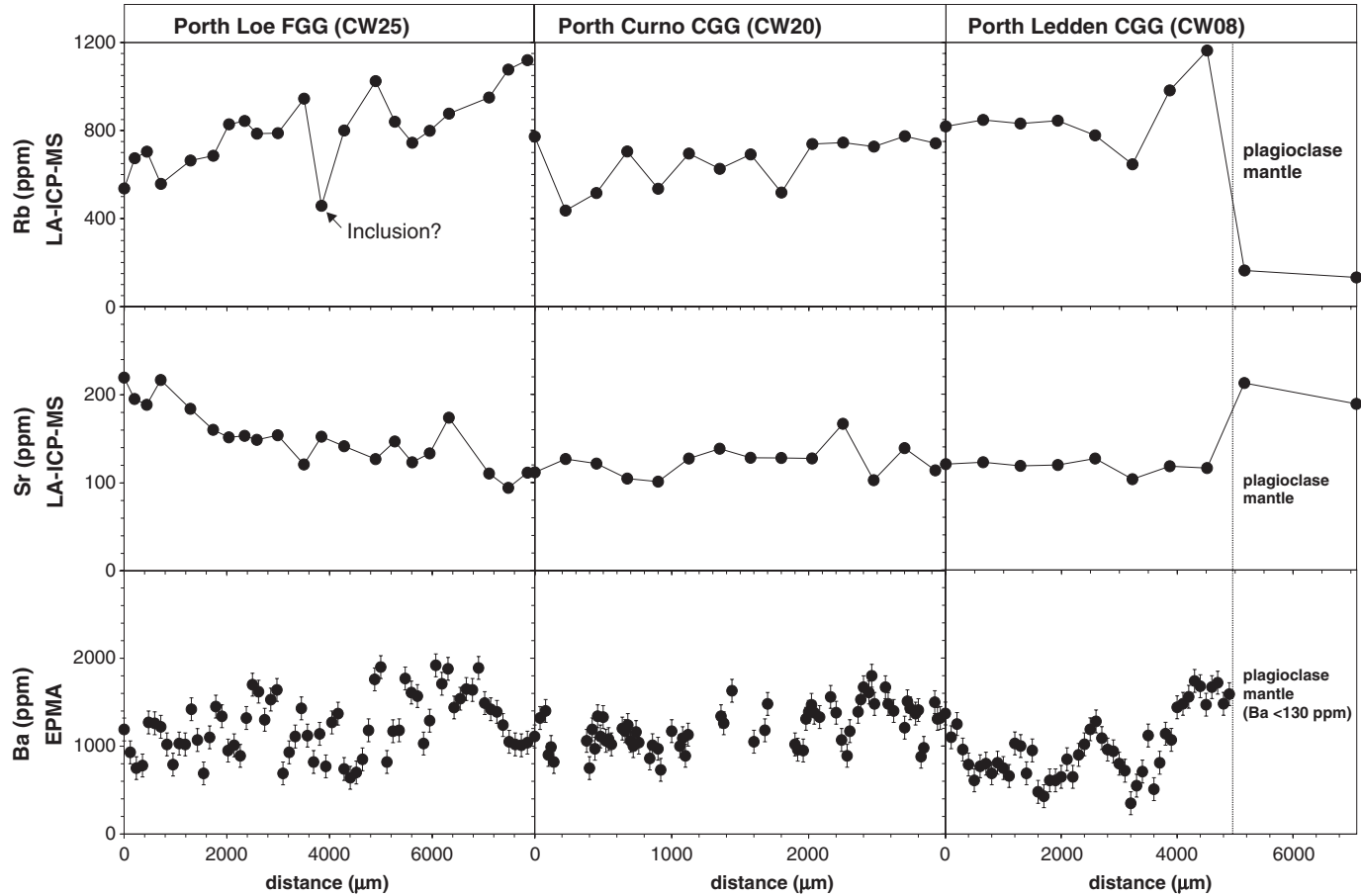
Fig. 10. Profiles of minor elements (Rb, Sr, Ba) in K-feldspar megacrysts from the FGG and CGG. Rb and Sr concentration were obtained by laser ablation ICP-MS and Ba by EPMA.
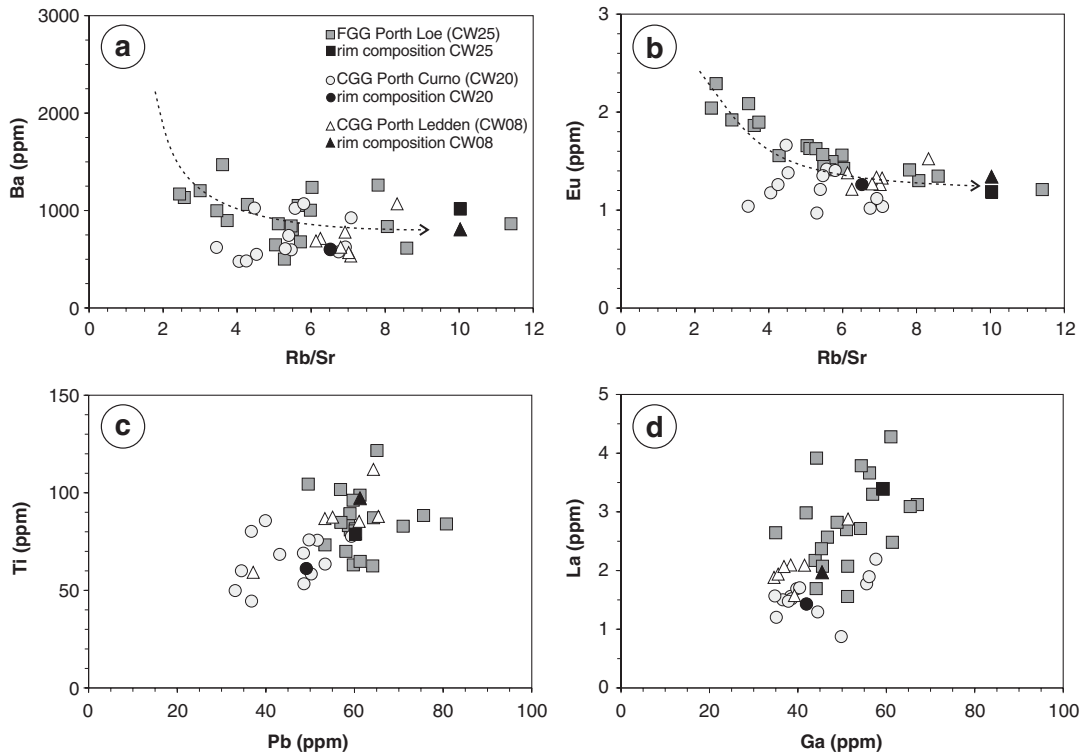
Fig. 11. Distribution of various elements in K-feldspar megacrysts from the FGG and CGG, which are indicative of magmatic differentiation. The data were collected with laser ablation ICP-MS. The arrows indicate the trend of trace element evolution in K-feldspar during progressive magmatic differentiation based on previous investigations (e.g., Larsen, 2002). The black symbols represent the composition of megacryst margins.

Li-siderophyllite granites, albite granite and tourmaline granites are relative rich in P (1000 and 1500 ppm), whereas the An-rich plagioclase cores of the FGG and CGG have lower P contents of 430 to 480 ppm.

4.3. Mica

The wide chemical variation of micas in the different granite units of the Land's End pluton provides
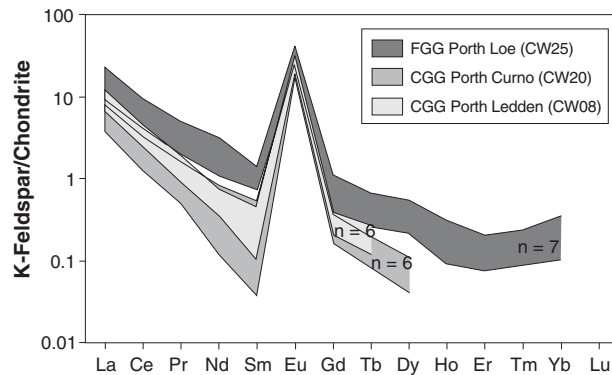

Fig. 12. Chondrite-normalised REE pattern of K-feldspar megacrysts from the FGG and CGG. The data were collected using laser ablation ICP-MS. The concentrations of HREE in the samples CW08 and CW20 are mostly below the limit of detection.

Table 5
Representative electron probe microanalyses of mica (wt.%)

Unit	FGG	FGG	CGG	CGG	CGG	CGG	Albite granite	Porph. Li-sideroph. granite	Porph. Li-sideroph. granite	Equigr. Li-sideroph. granite	Tourmaline granite	Tourmaline granite
Sample	CW25	CW25	CW20	CW20	CW08	CW08	CW67	CW11	CW11	CW31a	CW01	CW01
Mica	Mg-sideroph.	Fe-polylith.	Mg-sideroph	Fe-polylith.	sideroph.	Fe-polylith.	Fe-polylith.	sideroph.	Li-sideroph.	Li-sideroph.	Fe-polylith.	Li mus.
Sample#	10	14	3	4	4	2	37	6	18	9	8	11
SiO_2	34.75	44.85	34.47	44.92	36.09	45.39	45.09	37.01	39.26	40.21	45.94	45.73
TiO_2	3.86	0.28	3.39	0.43	2.46	0.51	0.02	1.81	1.25	1.15	0.06	0.14
Al_2O_3	18.02	33.99	18.91	34.41	18.85	33.04	33.77	21.06	21.62	23.65	34.60	36.21
FeO	22.89	1.32	22.86	1.42	20.61	2.62	1.41	19.36	16.23	15.25	2.84	0.50
MnO	0.29	0.02	0.22	0.02	0.29	0.04	0.02	0.30	0.26	0.29	0.01	0.10
MgO	5.07	0.82	4.56	0.85	4.88	1.28	1.07	2.35	2.72	1.57	0.17	0.20
CaO	<0.02	<0.02	0.02	0.05	0.02	<0.02	<0.02	<0.02	<0.02	<0.02	<0.02	<0.02
Li_2O calc	0.38	3.30	0.30	3.32	0.77	3.46	3.37	1.04	1.69	1.96	3.62	3.56
Na_2O	0.21	0.85	0.23	0.71	0.16	0.83	0.53	0.22	0.26	0.15	0.39	0.21
K_2O	9.62	10.70	9.75	10.91	9.88	10.62	11.08	9.85	9.41	9.25	9.52	9.98
Rb_2O	<0.10	<0.10	<0.10	<0.10	0.16	<0.10	0.12	0.25	0.33	0.33	<0.10	<0.10
Cs_2O	<0.09	<0.09	<0.09	<0.09	0.14	<0.09	<0.09	0.42	0.16	0.11	0.12	<0.09
F	1.17	0.54	1.84	0.62	3.02	2.38	0.14	4.01	4.42	4.23	0.37	<0.09
Cl	0.52	<0.07	0.37	<0.07	0.23	<0.07	<0.07	0.10	<0.07	0.04	<0.07	<0.07
sum	96.78	96.67	96.92	97.66	97.56	100.17	96.62	97.78	97.61	98.19	97.64	96.63
O=(F,Cl)	0.61	0.23	0.86	0.26	1.32	1.00	0.06	1.71	1.87	1.79	0.16	0.00
total	96.17	96.44	96.06	97.40	96.24	99.17	96.56	96.07	95.74	96.40	97.48	96.63
Cations												
Si	5.24	5.85	5.15	5.81	5.22	5.67	5.92	5.24	5.39	5.43	5.92	5.91
Ti	0.44	0.03	0.38	0.04	0.27	0.05	0.00	0.19	0.13	0.12	0.01	0.01
$Al^{(IV)}$	2.76	2.15	2.85	2.19	2.78	2.33	2.08	2.76	2.61	2.57	2.08	2.09
$Al^{(VI)}$	0.45	3.08	0.49	3.05	0.44	2.53	3.15	0.75	0.88	1.20	3.17	3.43
$Fe^{(II)}$	2.89	0.14	2.86	0.15	2.49	0.27	0.15	2.29	1.86	1.72	0.31	0.05
Mn	0.04	0.00	0.03	0.00	0.04	0.00	0.00	0.04	0.03	0.03	0.00	0.01
Mg	1.14	0.16	1.02	0.16	1.05	0.24	0.21	0.50	0.56	0.32	0.03	0.04
Ca	0.00	0.00	0.00	0.01	0.00	0.00	0.00	0.00	0.00	0.00	0.00	0.00
Li	0.23	1.73	0.18	1.73	0.45	1.74	1.78	0.59	0.93	1.07	1.87	1.85
Na	0.06	0.21	0.07	0.18	0.05	0.20	0.13	0.06	0.07	0.04	0.10	0.05
K	1.85	1.78	1.86	1.80	1.82	1.69	1.86	1.78	1.65	1.59	1.56	1.65
Rb	0.00	0.00	0.00	0.00	0.02	0.00	0.01	0.02	0.03	0.03	0.00	0.00
Cs	0.00	0.00	0.00	0.00	0.01	0.00	0.00	0.03	0.01	0.01	0.01	0.00
OH	3.31	3.78	3.04	3.74	2.56	3.06	3.94	2.18	2.07	2.19	3.85	4.00
F	0.56	0.22	0.87	0.25	1.38	0.94	0.06	1.79	1.92	1.80	0.15	0.00
Cl	0.13	0.00	0.09	0.00	0.06	0.00	0.00	0.02	0.01	0.01	0.00	0.00
Sum	19.10	19.14	18.89	19.12	18.63	18.73	19.30	18.24	18.15	18.12	19.06	19.09
Fe#	0.72	0.47	0.74	0.48	0.70	0.54	0.43	0.82	0.77	0.84	0.91	0.59

Li_2O_{calc} is calculated after Tischendorf et al. (2001).

CGG—medium- to coarse-grained porphyritic granite, equigr. Li-sideroph. granite—equigranular lithian siderophyllite granite, Fe-polylith.—ferroan polylithionite, FGG—fine-grained porphyritic granite, Li mus.—lithian muscovite, Li-sideroph.—lithian siderophyllite, Mg-sideroph.—magnesian siderophyllite, porph. Li-sideroph. granite—porphyritic lithian siderophyllite granite, sideroph.—siderophyllite
$Fe^{(II)}$ =total Fe as FeO, Fe#=tFe/(Mg+tFe).

an excellent criterion for distinguishing the separate stages of intrusion, particularly in the case of units which show similar macroscopic texture and whole-rock compositions (Table 5). The micas plot in three clusters in the $Fe+Mn+Ti–Al^{VI}$ vs. Mg–Li diagram of Tischendorf et al. (2001) (Fig. 13a).

Brown biotite (Mg-siderophyllite) predominates in the early FGG and CGG units. However, towards the north at Porth Ledden, the composition of the dark mica changes to siderophyllite (CGG CW08), indicating greater chemical differentiation. The siderophyllite of CW08 shows a high F content reaching up to 3 wt.%. The Al_2O_3 contents (18.8 to 18.9 wt.%) and tFe/(tFe+Mg) ratios (0.70 to 0.75) resemble those of biotites from the coarse-grained megacrystic granite of Dartmoor described by Stone (2000). The FGG and CGG also contain minor late- to post-magmatic Fe-polylithionite, which partially overgrows the biotite.

The Fe-polylithionite compositions plot predominantly in the field of secondary muscovite composition (Fig. 13b; Miller et al., 1981).

The porphyritic fine-grained granite with K-feldspar phenocrysts <3 cm and the equigranular tourmaline-bearing granite exposed in the cliffs from south of Porth Ledden to Porth Nanven are characterised by Li-siderophyllite. The Li-siderophyllite in these rocks has high concentrations of Rb_2O (0.3 to 0.4 wt.%), Cs_2O (0.11 to 0.16 wt.%) and F (4.2 to 4.5 wt.%). The porphyritic granite also contains minor brown siderophyllite, whereas the equigranular granite contains exclusively Li-siderophyllite.

The pink tourmaline granite of Porth Ledden and the albite microgranite contain Fe-polylithionite. Small micas found in the tourmaline granite are Li muscovite. Muscovites from the pink tourmaline granite plot in the field of primary muscovite (Fig. 13b; Miller et
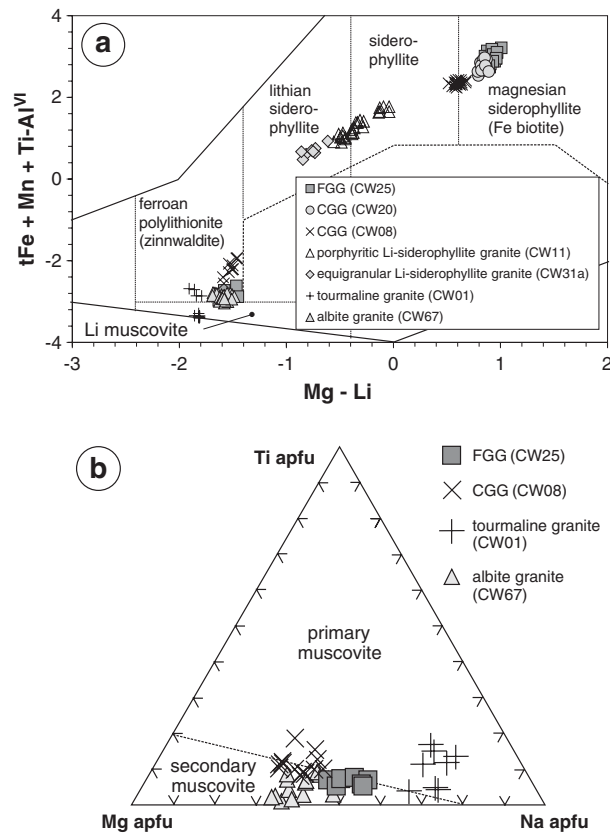

Fig. 13. (a) Position of micas from the main intrusive phases of the Land's End pluton plotted in the nomenclature diagram of Tischendorf et al. (2001). (b) Ferroan polylithionite and Li muscovite composition of the Land's End pluton plotted in the Na–Mg–Ti diagram (Miller et al., 1981). apfu—atoms per formula unit.

al., 1981) whereas the composition of the micas in albite granite corresponds to the composition of secondary muscovite. The composition of the primary micas changes progressively during differentiation.

4.4. Tourmaline

Tourmaline occurs in most of the granites of the Land's End pluton both as an accessory (FGG, CGG, Li-siderophyllite granites) and as a major rock-forming mineral (tourmaline granites, MQT). The formula of tourmaline and the name of sites used in this study follow the recommendations of Hawthorne and Henry (1999); $XY_3Z_6(T_6O_{18})(BO_3)_3V_3W$. The X site contains Na, Ca, K and vacancies (Xvac); the octahedral Y and Z site are occupied preferentially by the cations Li (Y), Fe^{2+}(Y), Mn^{2+}(Y), Mg, Al, Cr^{3+}, V^{3+}, $Fe^{3+}$and Ti^{4+}(Y). The B site is occupied exclusively by B, whereas the V and W sites contain OH^-, F^- and

O^{2-}. All tourmalines analysed belong to the alkali group.

Tourmalines are subhedral with dimensions of 20 to 4000 μm in cross-section perpendicular to the c-axis and 50 μm to 10 mm parallel to the axis. Accessory tourmaline in the FGG, CGG, and Li-siderophyllite granites shows simple zoning (2 to 5 growth zones) with maximum absorption colours of beige and brown. In the nomenclature diagram in Fig. 14a, the composition of the accessory tourmaline lies within the schorl field. It shows a wide variation in Mg/(Fe+Mg) ratio between 0.10 and 0.36 but tourmalines in the older granites (FGG, CGG) have the highest magnesium contents (Table 6). However, all compositions fall within the field of tourmalines from granites and pegmatites in SW England analysed by London and Manning (1995). Rock-forming tourmaline of the tourmaline granite and MQT at Porth Ledden has brown cores with moderate Mg/(Fe+Mg) (0.10 to
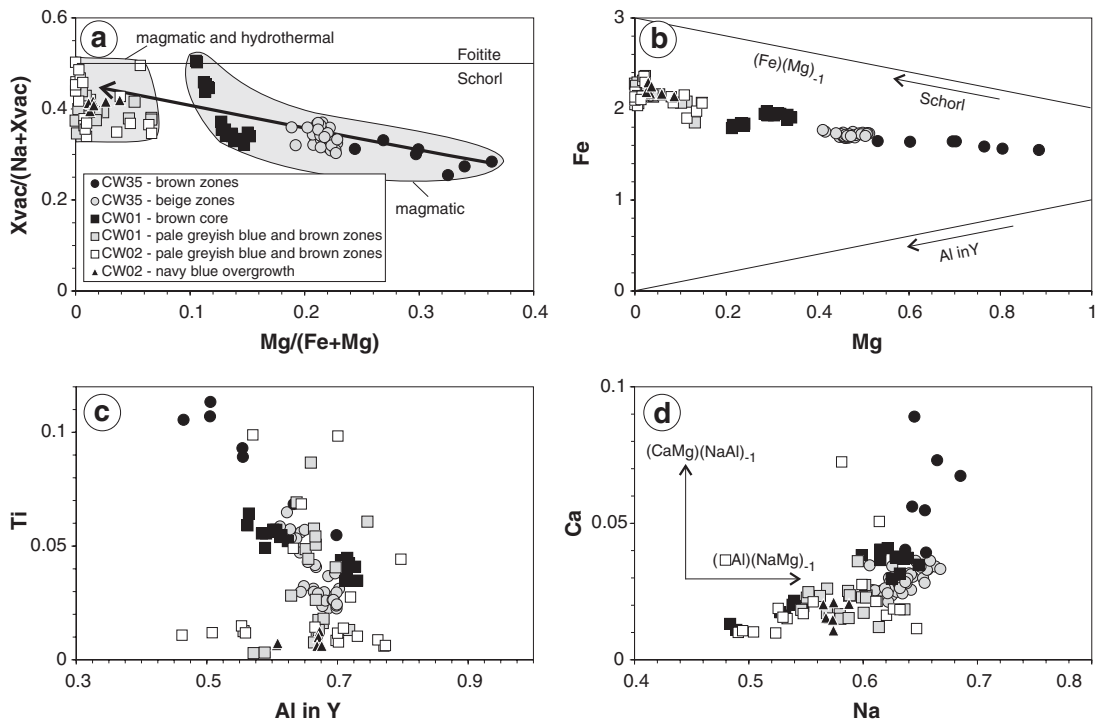

Fig. 14. Plots of cation occupancies (apfu) of tourmalines from the Land's End granites. (a) Nomenclature diagram of tourmalines. The arrow indicates the compositional trend of turmalines with increasing differentiation of the host rock. CW35—tourmaline-bearing Pellitras granite (CGG variety); CW01—pink tourmaline granite of Porth Ledden; CW02—MQT of Porth Ledden. (b) Plot of Fe vs. Mg. Schorl–dravite plot along the line $\sum$(Fe+Mg)=3; values of $\sum$(Fe+Mg+Mn+Ti)<3 correspond to Al substitution in the Y-site. (c) Plot of Al in Y vs. Ti. (d) Plot of Na vs. Ca.

Table 6

Representative compositions of tourmalines from the tourmaline-bearing Pellitras granite (CW35), pink tourmaline granite (CW01) and MQT of Porth Ledden (CW02)

	Tourmaline-bearing Pellitras granite (CW35)		Pink tourmaline granite (CW01)		MQT (CW02)	
Absorption colour	Beige zones	Brown zones	Brown core	Pale greyish blue zones	Pale greyish blue zones	Navy blue overgrowth
n[a]	29	7	18	17	7	7
Na_2O	1.98	2.04	1.78	1.78	1.73	1.74
CaO	0.17	0.34	0.15	0.12	0.09	0.09
K_2O	0.04	0.05	0.04	0.04	0.04	0.04
MgO	1.92	2.89	1.08	0.08	0.04	0.18
FeO	12.35	11.64	13.48	15.48	15.46	15.48
MnO	0.15	0.09	0.09	0.09	0.10	0.08
TiO_2	0.31	0.72	0.38	0.19	0.09	0.06
Al_2O_3	34.65	33.97	34.04	33.70	33.93	33.65
SiO_2	35.24	35.09	35.42	34.79	35.19	34.68
F	0.57	0.63	0.48	0.55	0.53	0.59
Li_2O[b]	0.06	0.08	0.24	0.09	0.13	0.03
B_2O_3[c]	10.48	10.50	10.43	10.26	10.33	10.22
H_2O[c]	3.35	3.32	3.37	3.28	3.31	3.25
$-O=F$	0.24	0.27	0.20	0.23	0.23	0.25
Total	101.03	101.09	100.79	100.21	100.74	99.84
Na	0.635	0.655	0.574	0.584	0.564	0.574
Ca	0.029	0.060	0.027	0.021	0.016	0.017
K	0.009	0.010	0.008	0.008	0.008	0.008
Mg	0.474	0.712	0.270	0.021	0.010	0.045
Fe	1.713	1.611	1.880	2.193	2.176	2.201
Mn	0.022	0.012	0.012	0.012	0.014	0.012
Ti	0.038	0.090	0.048	0.024	0.012	0.008
Al	6.770	6.629	6.688	6.727	6.726	6.743
Si	5.843	5.811	5.905	5.893	5.921	5.897
F	0.299	0.330	0.252	0.295	0.285	0.315
Li[b]	0.043	0.052	0.162	0.060	0.088	0.017
X	0.665	0.715	0.601	0.605	0.580	0.591
Y	2.208	2.335	2.162	2.226	2.200	2.258
Z	6.821	6.749	6.752	6.759	6.741	6.754
X+Y	2.873	3.050	2.763	2.831	2.779	2.848
Fe/Fe+Mg	0.783	0.695	0.875	0.991	0.996	0.980
XAl	0.664	0.559	0.657	0.653	0.662	0.651
Xvac	0.327	0.275	0.391	0.387	0.413	0.401

MQT—massive quartz tourmaline rock.

[a] Number of analyses.

[b] Li calculated using the method of Burns et al. (1994).

[c] B_2O_3 and H_2O calculated assuming fixed B at 3 atoms per formula unit (apfu) and (OH, F) at 4 apfu.

0.15). The brown cores are overgrown by oscillatory zoned tourmaline with pale greyish blue absorption colour and low Mg/(Fe+Mg) ratios <0.02. Some narrow zones have brownish colours and slightly higher Mg/(Fe+Mg) ratios of 0.03 to 0.07. The composition of the oscillatory zoned tourmaline plots in a narrow field in the nomenclature diagram clearly separated from the field of the brown cores and accessory tourmaline. All tourmaline populations are overprinted by a generation of navy blue tourmaline which forms small overgrowths and domains (<100 μm). Its composition resembles that of the oscillatory zoned tourmaline. Both populations are enriched in Fe and depleted in Mg, Ti and Ca. The decrease in Mg/(Fe+Mg) ratio reflects the progressive differentiation in the sequence of magma types, with the FGG being the least evolved

and the tourmaline granites being the most evolved. The compositional trend is mainly related to the coupled exchanges of $(Fe)(Mg)_{-1}$ (Fig. 14b). Minor differences of the composition are associated with the exchange vectors $(Al)_2(TiMg)_{-1}$, $(CaMg)(NaAl)_{-1}$, $(\square Al)(NaMg)_{-1}$ and $AlO(Mg,Fe)_{-1}(OH)_{-1}$, (Fig. 14c,d). The pleochroism is related to the $Fe/(Mg+Ti)$ ratio (Faye et al., 1974), which is 1.7 to 2.8 in the beige tourmaline (CW35), 3.0 to 7.3 in the brown tourmaline (CW35, CW01), 8.4–338.8 in the oscillatory, pale greyish blue tourmaline and 22.3 to 70.1 in the blue tourmaline.

4.5. Quartz

The anhedral quartz in the groundmass filling interstices between feldspar, tourmaline and/or mica in the equigranular Li-siderophyllite granite, tourmaline granites and MQT has an allotriomorphic texture. The FGG, CGG and porphyritic Li-siderophyllite granite contain quartz phenocrysts up to 1 cm in size embedded in finer grained anhedral groundmass quartz. SEM-CL reveals a weakly contrasted primary growth zoning of oscillatory character within quartz phenocrysts distinguishing them from the anhedral groundmass quartz. Using OM-CL, major growth zones are distinguished by blue, violet and red-brown colours (Fig. 3d), but the fine-scale oscillatory zoning is only visible with SEM-CL.

The phenocrysts and the anhedral quartz of the groundmass show a dense network of thin, healed cracks (usually < 5 μm) connecting irregular domains (usually 5 to 100 μm) of weak red-brown luminescing quartz denoted "sqz" in Fig. 15a. The irregular domains envelope fluid inclusions. Such structures are characteristically of quartz within plutonic rocks (e.g., Sprunt and Nur, 1979; Behr and Frentzel-Beyme, 1989; Valley and Graham, 1996). Secondary

quartz in Fig. 15a is dark grey (dark red-brown in OM-CL). In Fig. 16b, the CL of this quartz has changed to bright grey (orange in OM-CL) due to several minutes of electron beam exposure.

The SEM-CL images in Figs. 15a and 16b show the textural relationship of quartz and tourmaline (black) in the MQT from Porth Ledden. Bluish to violet luminescing magmatic quartz (mqz) shows as bright grey in Fig. 15a contains a dense network of secondary quartz (sqz) which is overgrown by quartz showing fine-scale zoning (hqz) where porous open spaces remained to be filled. These overgrowths develop euhedral crystal forms of low-quartz habit in places with suffcient space. Melt inclusions occurring within the bluish luminescing quartz are evidence of its magmatic origin (Müller et al., submitted for publication). The bluish to violet luminescing magmatic quartz of the MQT is occasionally overprinted by irregular patches of reddish luminescing quartz ("amqz" in Figs. 3e and 15a) leading off from grain boundaries. The oscillatory zoned overgrowth exhibits sector zoning (Fig. 15a) and it is almost free of secondary structures. The individual growth zones have greenish brown to yellowish brown and dull red CL.

Abundances of the trace elements Al, K, Ti, and Fe along traverses in a zoned quartz phenocryst from the Li-siderophyllite granite and quartz from the MQT (Fig. 16) were analysed. The blue luminescing core of the quartz phenocryst (Fig. 3d) contains higher Ti concentrations (120 to 168 ppm) than the overgrowth (47 to 100 ppm). The Al contents of the core and overgrowth are similar, ranging between 425 and 478 ppm (Fig. 16a). The concentration peaks of 627 and 654 ppm are attributed to microscopic silicate inclusions. The trace element traverse of quartz from the MQT crosses four quartz types with different CL properties and chemical signatures. These are: (a)

Fig. 15. (a) SEM-CL image of quartz (mqz, sqz, hqz) and tourmaline from the MQT. For explanation see text. (b) Backscattered electron (BSE) image of zircon from the FGG (CW24) showing two crystal nuclei in the core. (c) BSE image of zircon from the MQT (CW02) with altered and pitted crystal margin. (d) BSE image of zircon from the albite microgranite (CW67). (e) Combination of two BSE images of monazite–(Ce) (background image) with corroded zircon inclusions (zir; inserted from a BSE image with different contrast to reveal internal zoning) from porphyritic Li-siderophyllite granite (CW44). The two bright areas (white arrows) have monazite–(Nd) composition. (f) BSE image of monazite–(Ce) and uranothorite found in the equigranular Li-siderophyllite granite (CW31b). The irregular zoning of the monazite results from redistribution of heavy elements, e.g., thorite. (g) Homogenised melt inclusion from the FGG (held at 850 °C and 2 kbar for 24 h). They consist of a silicate glass, vapour phase and a saline phase with a halite crystal. (h) Drop-like sulphide inclusion associated with other solids (arrows) and a vapour phase in quartz from the CGG (CW20). Transmitted plane-polarised light. (i) BSE image of a drop-like sulphide inclusion in quartz from the porphyritic Li-siderophyllite granite (CW44).

magmatic quartz (mqz), (b) altered magmatic quartz (amqz), (c) secondary quartz in healed cracks and domains around fluid inclusions (sqz), and (d) euhedral overgrowths (hqz) with oscillatory zoning (Fig.

16b). The content of Ti in the four quartz types is below the detection limit of 33 ppm. Magmatic quartz has between 378 and 508 ppm Al but Al is lower in the altered parts (75 to 280 ppm). The euhedral over-
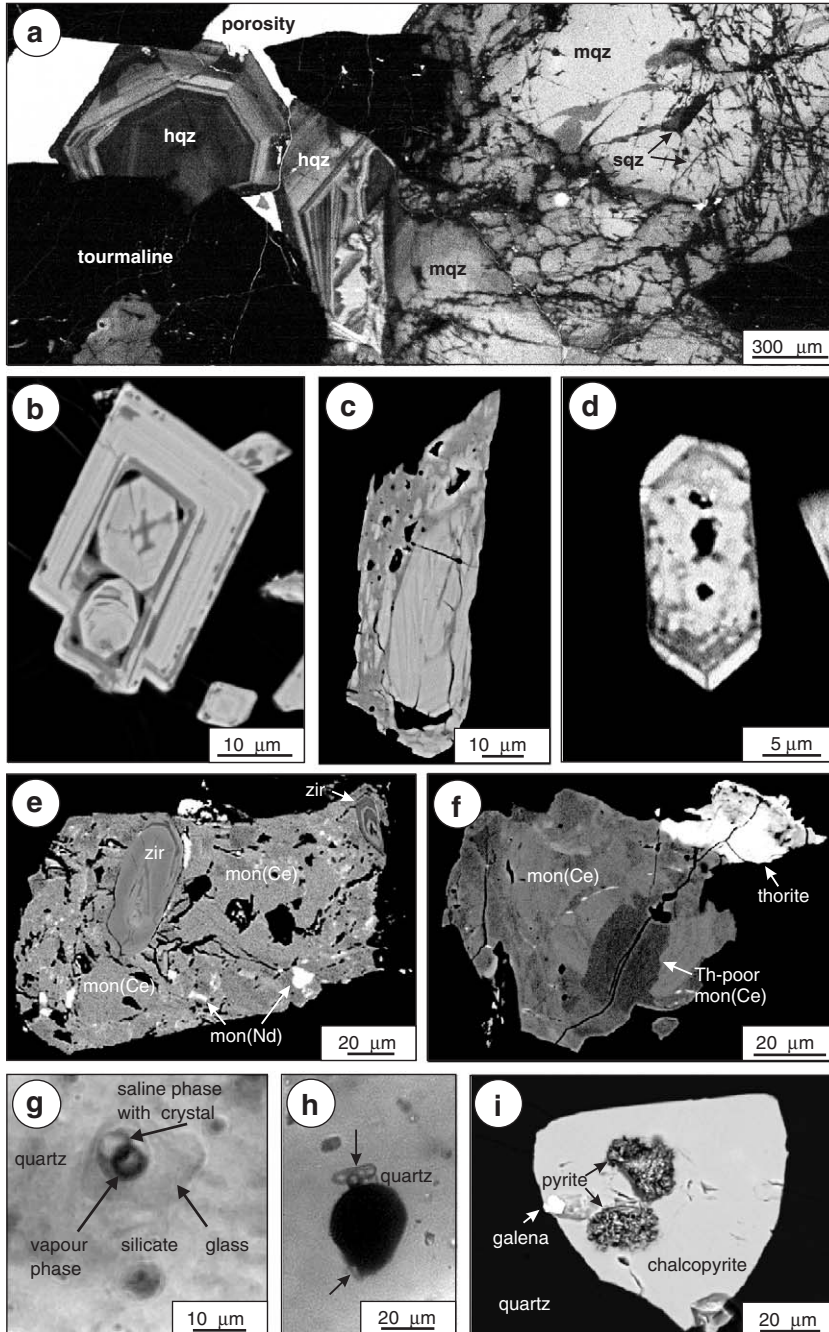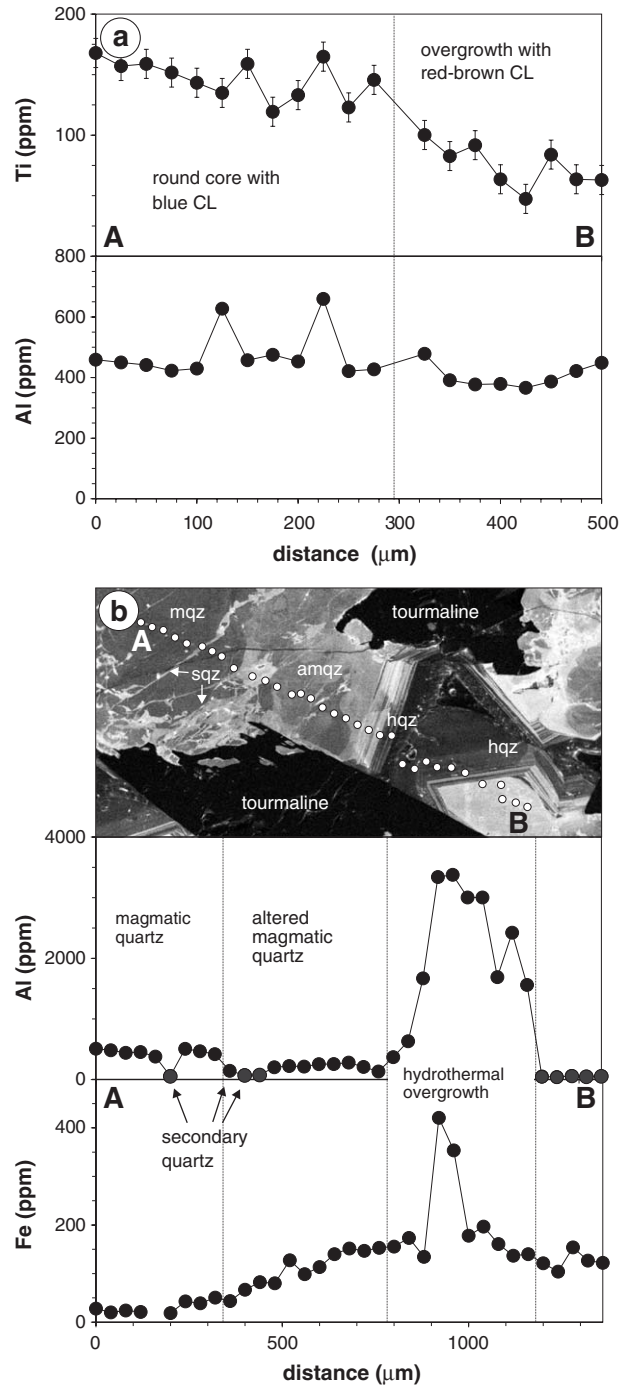
Fig. 16. Trace elements in quartz from (a) porphyritic Li-siderophyllite granite (CW44) and (b) MQT (CW02). The scanning electron microscope cathodoluminescence image in (b) reveals the textural relationships between magmatic quartz (mqz), altered magmatic quartz (amqz), secondary quartz (sqz), hydrothermal quartz (hqz) and tourmaline. The secondary quartz which appears black in the SEM-CL image at initial electron bombardment (see Fig. 15a) turns into bright grey after several minutes of electron radiation.

growth (hqz) contains up to 3500 ppm Al. Magmatic quartz has between 28 and 43 ppm Fe. Iron increases in the altered domains (amqz) towards the grain margins from about 40 to 150 ppm. Fe in the overgrowth ranges mostly between 130 and 200 ppm, but the final, dull red luminescing growth zone has up to 420 ppm Fe.

4.6. Accessory minerals

Zircons of the CGG, FGG, Li-siderophyllite granites and tourmaline granites show regular oscillatory zoning of cores and margins (Fig. 15b). The core and margin are separated by a thin growth zone which has lower concentrations of heavy elements and appears darker in the BSE image. The zircons included in monazite are strongly corroded, as revealed by truncated zoning (Fig. 15e). As the degree of differentiation increases, the zircons become increasingly altered along the rims resulting in marginal pitting of the grains (Fig. 15c). Zircons in the albite granite are small <20 μm and have characteristic patchy cores overgrown by thin oscillatory zoned margins (Fig. 15d). Generally, Zr/Hf ratios are relatively constant,

with a mean value of ~38 (Table 7), which is typical for magmatic zircons from peraluminous granites of mainly crustal derivation (Pupin, 2000). The Fe, Y, Th, U and HREE contents in the zircons from the different granites vary, but do not show any systematic trends.

The composition and morphology of *apatites* from the different granite units varies markedly (Table 8). The FGG, CGG, Li-siderophyllite granites and tourmaline granites contain Cl- and OH-poor fluorapatite. The early-magmatic apatite of the FGG and CGG is relatively rich in Na, Fe, Mn and LREE and shows a homogeneous bright yellow cathodoluminescence (CL). In some cases the crystals, up to 1 mm in size, have a nearly euhedral shape. Na vs. (La+Ce) in apatite from FGG, CGG and Li-siderophyllite granites plot in the same field (Fig. 17), indicating a similar degree of differentiation in the separate melts and a similar assemblage of REE-minerals co-existing at the time of apatite crystallisation. Apatites from the albite microgranite and from the tourmaline granites contain lower amounts of LREE and Na. The albite microgranite contains hydroxylapatite, which is unusual in magmatic rocks (Chang et al., 1996). How-

Table 7
Representative electron probe microanalyses of zircon (wt.%)

Unit	FGG		Albite granite	Porphyr. Li-sideroph. granite		Equigr. Li-sideroph. granite		MQT
Sample	CW24	CW24	CW67	CW44	CW44	CW31b	CW31b	CW02
Crystal	Core	Rim	Core	Core	Rim	Core	Rim	Core
Sample #	8	9	3	5	6	1	3	11
SiO_2	32.90	33.20	32.39	32.25	32.33	32.65	32.58	31.82
ZrO_2	63.85	65.33	66.75	65.83	66.53	67.02	66.44	65.23
HfO_2	1.28	1.50	1.99	1.30	1.55	1.36	1.27	1.86
ThO_2	0.28	<0.17	<0.17	<0.17	<0.17	<0.17	<0.17	<0.17
UO_2	0.25	0.36	0.45	<0.19	<0.19	<0.19	<0.19	0.54
Al_2O_3	0.20	<0.04	<0.04	<0.04	<0.04	0.07	<0.04	<0.04
Y_2O_3	0.87	0.65	<0.51	<0.51	<0.51	<0.51	<0.51	<0.51
Dy_2O_3	0.19	<0.10	<0.10	0.11	<0.10	0.11	<0.10	<0.10
Er_2O_3	0.13	0.20	<0.10	<0.10	<0.10	<0.10	<0.10	0.13
Yb_2O_3	0.11	0.25	0.14	<0.10	<0.10	0.27	<0.10	<0.10
CaO	0.07	<0.02	0.02	<0.02	<0.02	<0.02	<0.02	0.02
tFeO	0.88	0.61	<0.08	0.30	0.41	<0.08	<0.08	<0.08
Total	101.01	102.10	101.74	99.79	100.82	101.48	100.29	99.60
Zr/Hf_W	43.1	45.9	43.4	38.1	30.7	29.2	44.4	37.5

Equigr. Li-sideroph. granite—equigranular lithian siderophyllite granite, FGG—fine-grained porphyritic granite, MQT—massive quartz tourmaline rock, porphyr. Li-sideroph. granite—porphyritic lithian siderophyllite granite.
tFeO total Fe as FeO.
Zr/Hf_W calculated from atomic weights.

Table 8
Representative electron probe microanalyses of apatite (wt.%)

Unit	FGG	Albite granite	Porph. Li-sideroph. granite	Equigr. Li-sideroph. granite	Tourmaline granite
Sample	CW24	CW67	CW44	CW31b	CW02
Sample#	12	8	2	15	3
SO_3	<0.17	<0.17	<0.17	<0.17	<0.17
P_2O_5	42.70	42.80	41.65	41.66	43.12
CaO	53.93	55.23	54.64	53.58	56.77
ThO_2	<0.17	<0.17	<0.17	<0.17	<0.17
UO_2	<0.19	<0.19	<0.19	<0.19	<0.19
La_2O_3	0.09	<0.07	0.08	0.07	<0.07
Ce_2O_3	0.23	0.16	0.24	0.22	0.11
SrO	<0.05	<0.05	<0.05	<0.05	<0.05
tFeO	1.11	0.70	0.50	0.85	0.28
MnO	1.52	0.83	1.16	0.67	0.58
Na_2O	0.21	0.12	0.17	0.21	0.05
F	2.20	0.14	2.22	1.85	1.99
Cl	0.07	0.17	<0.07	0.21	<0.07
H_2O[a]	0.72	1.67	0.70	0.76	0.84
O=(-			(F + Cl)	0.94	0.10
0.95	0.82	0.84			
Total	101.84	101.72	100.41	99.26	102.90

Equigr. Li-sideroph. granite—equigranular lithian siderophyllite granite, FGG—fine-grained porphyritic granite, porph. Li-sideroph. granite—porphyritic lithian siderophyllite granite.
tFeO total Fe as FeO.

ever, the irregular large apatites (up to 1 mm) seem to be magmatic in origin because they have relatively high contents of Fe, Na and LREE and low contents of Mn and Sr (e.g., Chang et al., 1996). Alteration of zoned magmatic apatite is revealed by CL. Altered

zones are depleted in Na, Si and Y + REE, which is in agreement with experimental results (Harlov et al., 2002). In Fig. 3f, a CL image of apatite from the pink tourmaline granite (CW01) is shown. The unaltered apatite (grey and dark grey areas) shows primary euhedral zoning picked out predominantly by variations in Mn content (Kempe and Götze, 2002). This is overprinted by a later phase of bright yellow luminescing apatite with a higher Mn content. The primary zoning of the apatite in the MQT is completely overprinted (Fig. 3g).

The *monazite*–(Ce) from the Land's End granites shows considerable variation in the contents of Y, Th and Ca, but La_N/Ce_N and Nd_N/Sm_N are relatively constant, indicating generally similar states of differentiation in the granite magmas and similar associations of crystallizing minerals (Table 9). Crystal margins and, sometimes, domains within the crystals are converted to allanite-like compositions showing felted textures. The areas of allanite-like composition are probably the result of chloritisation and/or sericitisation (Ward et al., 1990; Eliasson and Petersson, 1996; Poitrasson et al., 2000). Monazite–(Nd) forms domains within monazite–(Ce) crystals in the porphyritic Li-siderophyllite granite.

4.7. Melt inclusions and sulphide inclusions in magmatic quartz

Crystallised melt inclusions in the Land's End granites are rare and they are hard to distinguish
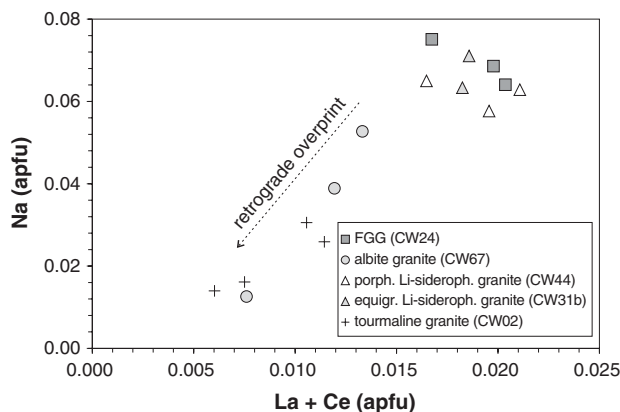

Fig. 17. Plot of Na vs. (La+Ce) (atoms per formula unit) of apatite from different granites of the Land's End pluton. The arrow emphasises Na and REE decrease with progressive retrograde overprinting of the early-magmatic apatite as a result of deuteric processes.

Table 9
Representative electron probe microanalyses of monazite (wt.%)

Unit	Limit of detection	FGG	Porph. Li-sideroph. granite		Equigr. Li-sideroph. granite
Sample		CW24	CW44	CW44	CW31b
Mineral		Monazite–(Ce)	Monazite–(Ce)	Monazite–(Nd)	Monazite–(Ce)
Analysis #		18	6	4	7
P_2O_5	0.12	29.03	28.73	27.02	26.83
SiO_2	0.03	0.46	0.61	1.23	0.55
ThO_2	0.14	9.64	1.86	0.51	3.29
UO_2	0.19	1.26	<0.19	<0.19	<0.19
Y_2O_3	0.22	2.23	0.55	0.72	0.39
La_2O_3	0.19	11.52	13.86	2.32	12.59
Ce_2O_3	0.19	25.88	29.28	15.63	30.81
Pr_2O_3	0.47	2.95	3.43	4.49	3.67
Nd_2O_3	0.49	10.83	14.83	30.06	14.05
Sm_2O_3	0.34	2.01	3.74	11.02	2.56
Eu_2O_3	0.23	<0.23	0.35	0.83	<0.23
Gd_2O_3	0.29	1.38	2.22	4.18	1.53
Dy_2O_3	0.38	1.05	1.57	<0.38	0.53
Er_2O_3	0.29	<0.29	<0.29	<0.29	<0.29
Yb_2O_3	0.30	<0.30	<0.30	<0.30	<0.30
Al_2O_3	0.04	0.04	0.13	<0.04	<0.04
CaO	0.05	1.82	0.14	<0.05	0.48
FeO	0.02	0.12	0.14	0.07	0.06
PbO	0.14	<0.14	<0.14	<0.14	<0.14
Total		100.22	101.44	98.08	97.34
La_N/Ce_N		1.14	1.21	0.38	1.05
Nd_N/Sm_N		1.72	0.88	0.72	1.75

Equigr. Li-sideroph. granite—equigranular lithian siderophyllite granite, FGG—fine-grained porphyritic granite, porph. Li-sideroph. granite—porphyritic lithian siderophyllite granite.

La_N/Ce_N=La(chondrite normalised)/Ce(chondrite normalised).

Nd_N/Sm_N=Nd(chondrite normalised)/Sm(chondrite normalised).

within the dense network of fluid inclusion trails penetrating the host quartz. The spherical to hexagonal melt inclusions of the CCG, FGG and Li-siderophyllite granite are usually 5 to 35 μm in diameter and contain a small volatile bubble or no bubble at all, and occasionally visible biotite and apatite crystals. Crystallised melt inclusions of the MQT have an irregular shape and are 5 to 20 μm in size. They contain silicate phases, a vapour phase and occasionally halite crystals. Fig. 15g shows a quenched melt inclusion in quartz from the FGG which was held at 850 °C and 2 kbar for 24 h using CO_2 as the pressure medium (Müller et al., submitted for publication). The inclusion consists of three non-quenchable phases: silicate glass, a vapour and aqueous phase with a halite daughter crystal. Such melt inclusions are evidence for co-existence of an immiscible hydrous sa-

line melt with the silicate melt (e.g., Roedder, 1992). The ratio of silicate glass/saline aqueous phase in the multi-phase melt inclusions decreases with increasing degree of differentiation of the granite host (Müller et al., submitted for publication). Silicate glass compositions of melt inclusions from different granites are listed in Table 10. The SiO_2 content of the glass is consistently 3 to 5 wt.% higher than the whole-rock value. On the other hand, the alkali concentrations in melt inclusions from the FGG and Li-siderophyllite granites are lower than the whole-rock content. In contrast, the melt inclusion glass from the MQT contains much more Na and K than the whole rock. The silicate glass of the melt inclusions contains chlorine in concentrations as high as 0.3 wt.%, whereas F is below the detection limit of 0.1 wt.%, which explains the absence of topaz in the Land's End granites.

Table 10

Electron probe microanalyses of homogenised silicate glass from melt inclusions (MI) in Land's End granites

	FGG (CW25)	Lithian siderophyllite granite (CW32)	MQT (CW02)
MI number	MI 3b	MI 8	MI 7
n	1	2	4
SiO_2	76.38	77.88 ± 0.16	78.55 ± 0.15
TiO_2	0.11	0.09 ± 0.01	0.10 ± 0.04
Al_2O_3	12.46	12.39 ± 0.04	11.41 ± 0.12
FeO	0.80	0.94 ± 0.08	0.69 ± 0.16
MgO	0.14	0.04 ± 0.01	0.08 ± 0.01
MnO	<0.09	<0.09	<0.09
CaO	0.81	0.43 ± 0.04	0.33 ± 0.02
K_2O	1.34	0.52 ± 0.04	1.23 ± 0.14
Na_2O	1.27	1.41 ± 0.08	1.7 ± 0.06
Rb_2O	<0.14	<0.14	<0.14
P_2O_5	<0.12	<0.12	<0.12
Cl	0.33	0.27 ± 0.02	0.27 ± 0.01
F	<0.10	<0.10	<0.10
O=Cl,F	0.07	0.06	0.06
Total	93.63	93.95	94.3
H_2O	6.4	6.0 ± 0.1	5.7 ± 0.1

FGG—fine-grained porphyritic granite, MQT—massive quartz tourmaline rock, n—number of analyses. Data from Müller et al. (submitted for publication).

Drop-like micro-inclusions of chalcopyrite and pyrite are common in quartz from the porphyritic Li-siderophyllite granites between Porth Ledden and Porth Nanven (Fig. 15h,i). The sulphide inclusions consist mainly of chalcopyrite together with minor pyrite and occasionally small galena crystals. Because they are enclosed within the zoned magmatic quartz phenocrysts (Fig. 3d) it is assumed that these drops were most probably trapped during the magmatic stage. This suggests that they could be remnants of an exotic sulphide melt co-existing with the silicate magma. Similar sulphide inclusions were described in rhyodacites from the Urals by Naumov et al. (1999).

5. Discussion

Although some investigators have opted for ultimate derivation of the Cornubian plutons from the mantle with some assimilation of crust (Watson et al., 1984; Leat et al., 1987; Stimac et al., 1995), others favour production of the granites from a tectonically overthickened crust (Shackleton et al., 1982) or through crustal melting initiated by mantle-derived melts (Chesley et al., 1993). A dominantly crustal source for the Cornubian granites is implied by Sr, Nd, Pb and $\delta^{18}O$ isotope data (Sheppard, 1977; Hampton and Taylor, 1983; Darbyshire and Shepherd, 1994). The isotopic ratios of the samples from the Land's End pluton which have been investigated are in the range of compositions expected for melts derived from a crustal source. The Nd model ages (1.5 to 1.7 Ga, Table 3) are similar to the basement of southern Britain (Hampton and Taylor, 1983; Davies et al., 1985) and imply derivation of the melt from a Proterozoic crustal precursor. Apart from areas of extensive hydrothermal alteration (localities of samples CW44 and CW01), the initial $^{87}Sr/^{86}Sr$ ratios from the Land's End samples as well as the $\varepsilon_{Nd}(t)$ values still seem to be a reliable indication of a crustal source.

The genetic relationship between the Land's End biotite granites and the albite microgranite is not straightforward. Compared to the two analysed biotite granite samples, the albite microgranite sample is characterised by a significantly higher $^{87}Sr/^{86}Sr$ ratio and a lower $\varepsilon_{Nd}(t)$ value. The data imply that the albite microgranite was more strongly affected by crustal assimilation and this would be in line with the derivation of this sample from the roof zone of the magma chamber. If assimilation was involved, the assimilant must have been either a mafic rock or a plagioclase-rich cumulate as indicated by the comparatively low Rb/Sr ratio (Table 3), the positive europium anomaly and the other geochemical features of the albite microgranite described above. A mafic input, however, does not seem compatible with the isotope data. Assimilation, if it took place, must have involved very old mafic or plagioclase dominated material (only these would have had more radiogenic Sr and non-radiogenic Nd ratios). Alternatively, a separate magma source must be invoked for the albite microgranite.

5.1. Compositional zoning of K-feldsparmegacrysts— record of the early and main magmatic stages

The tendency for progressive changes of Rb, Sr and Ba from core to rim in the K-feldspar megacrysts indicates that crystallisation of the phenocrysts took place in an evolving magma, probably over a long

period. The FGG megacrysts, in particular, show the greatest variation between core and rim compositions. This intra-granular heterogeneity contrasts with the relatively minor variation of the whole-rock composition throughout the older Land's End granites. This implies that the distribution of elements within the megacrysts also ought to be more uniform. The elements Rb, Sr and Ba in K-feldspar are sensitive to igneous differentiation (Mehnert and Büsch, 1981; Long and Luth, 1986; Cox et al., 1996) and the REE distribution in K-feldspar from granites also follows a well-defined evolutionary path during igneous differentiation (Larsen, 2002). Thus, differences in magma origin and evolution should result in different REE patterns. The similarity of REE patterns and Rb/Sr ratios may indicate that crystallisation of the megacrysts generally took place within a moderately evolved magma, the composition of which is probably close to that of the FGG enclaves at Porth Ledden. However, somewhat higher REE and Sr in the core zones of the FGG megacryst implies that they originated within a more evolved magma than the CGG megacrysts did. The marginal growth zones of the FGG megacryst are similar to the average composition of the CGG megacrysts. This suggests that the compositions of the FGG and CGG magmas are linked in their chemical evolution. Minor differences between the trace element patterns of individual megacrysts indicate that they crystallised in different magma batches and/or at different times. The megacrysts of the CGG exhibit a more evolved and more homogeneous composition, and are probably younger.

The progressive tendency in chemical evolution of the magma is also documented by the decrease in Ti content from core to rim in quartz phenocrysts, because elevated Ti in magmatic quartz is indicative of a hotter and less-evolved environment of crystallisation (Müller et al., 2003a).

Megacrystic rapakivi feldspars (plagioclase-mantled K-feldspars) are present in the FGG and CGG. Traditionally, the plagioclase-mantled potassium feldspar in Proterozoic rapakivi granites has been explained as a result of mixing with a more mafic (basaltic) magma (Hibbard, 1981; Wark and Stimac, 1992) and/or as an effect of isothermal decompression of the granite melt (Nekvasil, 1991; Eklund and Shebanov, 1999). Adiabatic magma ascent (isothermal decompression) in late-orogenic environments is a common process but it is difficult to understand why rapakivi feldspars are so rare. The slight increase of Ba at the margin of K-feldspar megacrysts may be evidence for a slight increase of the temperature of the melt due to mixing with a hotter batch of magma (Long and Luth, 1986). However, the increase in Ba is too low to be used as evidence for mixing with a much less evolved magma (Müller et al., 2003b). Also, the typical disequilibrium textures described, e.g., by Hibbard (1991) produced when mixing with mafic magma takes place are missing. However, studies by Stimac et al. (1995) and Shail et al. (2003) provide evidence that mantle-derived magmas may have underplated and/or been injected into the Cornubian crustal batholith. In the case of multiple recharge and intrusion of FGG and CGG sub-stages, as in the Pellitras granite, a local increase of temperature may have resulted in the nucleation of plagioclase around K-feldspar megacrysts. The plagioclase mantle, consisting of a mosaic of hundreds of small plagioclase crystals, indicates that synneusis of plagioclase crystals may have taken place at the K-feldspar surface under conditions of turbulent magmatic flow (Vance, 1969) so contributing to the formation to the mantle.

5.2. Compositional zoning of quartz and tourmaline— a record of the late-magmatic/hydrothermal transition

The characteristic feature of the Pellitras and Lisiderophyllite granites is the marked enrichment of boron together with silica and alkalies resulting from in situ fractionation and filter pressing in the apical parts of the intrusive bodies. Due to the enrichment of boron in the magma, the melt viscosity (e.g., Dingwell et al., 1992) and the solidus decreased markedly (e.g., Pichavant, 1979) which enhances and extends the differentiation process.

The compositional section across the sheet-like Pellitras granite intrusion (Fig. 8) illustrates the in situ enrichment of B, Sn and Cu within a relatively small magma volume. Increasing B and Cl concentrations in the melt promote increasing metal solubility, though boron is not necessarily directly involved in the transport and concentration of tin. Chlorine-bearing phases are highly efficient in transporting Sn and Cu from magmas and rocks (Heinrich, 1990; Lehmann, 1990; Keppler and Wyllie, 1991; Taylor and Wall, 1993; Müller and Seward, 2001). Evidence for

the unmixing of the saline phase from the silicate phase is recorded in the melt inclusions of all intrusion stages (Müller et al., submitted for publication) since Cl is not an essential constituent of the crystal structure of the main rock-forming minerals and it will concentrate in the residual fluid together with H_2O during magma differentiation. Several theoretical and experimental studies have shown that a dense, highly saline fluid ($\pm$ a lower density, lower-salinity "vapour" phase) can coexist with silicate melts of granitic composition (e.g., Shinohara et al., 1989; Candela, 1989).

The average boron content of the Devonian metasediments is 100 ppm (Hall, 1990). Pelitic rocks similar to the metasediments are assumed to be the main protoliths of the Cornubian magmas (e.g., Jackson et al., 1982). This "initial" boron value is sufficient to explain the boron content of the Land's End magmas because magmatic differentiation can increase the boron content by over an order of magnitude (Lehmann et al., 2000). Dingwell et al. (1996) suggested that the maximum B_2O_3 content of leucogranitic melts coexisting with schorl–dravite tourmaline, as occurs in the Land's End granites, is close to 0.5 wt.% B_2O_3. Excessive boron is partitioned towards the hydrous fluid (Pichavant, 1981) forming a transitional hydrous borosilicate phase coexisting with melts. Locally, these boron-enriched phases became segregated to form small irregular intrusive stocks and tongues (<300 m) of tourmaline granite within the pluton, preferentially near the contact with the Devonian Mylor Formation. Lesser degrees of unmixing locally have led to the formation of fine-grained, cm-sized tourmaline–quartz patches within the granites. Boron is also responsible for the partitioning of the alkalies (Pichavant, 1979). Potassium mostly resides in the melt and sodium partitions in the vapour phase in equilibrium with it (Charoy, 1982). The MQT rock of Porth Ledden is thought to be the end product of unmixing of a boron-, alkali-, silica-rich phase from the Land's End granites (Charoy, 1982). At the final stage of unmixing the borosilicate phase separates from the potassium-rich phase so that the MQT then co-exists with a monofeldspathic syenite. Boulders of monofeldspathic syenite are described by Charoy (1979) from Porth Ledden. The field evidence for a magmatic origin of the MQT (Charoy, 1982) is, however, not supported by experimental studies (e.g., Manning, 1981).

Our results and the investigations by Power (1968), Manning (1985) and Farmer and Halls (1993) suggest that with evolution of the granite system towards the pneumatolytic/hydrothermal stage, there is a corresponding decrease in the Mg/(Fe+Mg) ratio in tourmalines. Also the decreasing Ti in tourmaline reflects the progressive differentiation within the sequence of magma types, with FGG being the least evolved and tourmaline granites and MQT being the most evolved. The formation of accessory brown tourmaline in the FGG, CGG and the Li-siderophyllite granites is clearly a product of crystallisation from the magma as proposed by Charoy (1982) and Farmer and Halls (1993). The smooth transition from moderate to low Mg/(Mg+Fe) and the textural relationships (tourmaline crystallised prior to magmatic quartz) also suggest a magmatic origin for the pale greyish blue tourmaline of the tourmaline granite and MQT from Porth Ledden. The secondary overgrowth of navy blue tourmaline occurring in all rocks is assumed to be hydrothermal (e.g., Charoy, 1982; London and Manning, 1995; Williamson et al., 2000) despite the fact that its composition is similar to the composition of the magmatic pale greyish blue tourmaline (Fig. 10b).

CL properties, the patterns of variation of trace elements and the inclusion inventory indicate that most of the quartz in the MQT crystallised from a silica-rich melt. Magmatic quartz forms 90 to 95 vol.% of the total quartz of the MQT. Quartz overgrowth with planar oscillatory zoning, sharp crystal edges, sector zoning and low-quartz habit constitutes the remaining 5 to 10 vol.%. These features are typical for quartz crystallised from an aqueous fluid (e.g., Ramseyer and Mullis, 1990; Götze et al., 2001). The high Al content reaching up to 3,500 ppm is an additional indication of the hydrothermal origin of the overgrowths (e.g., Mullis and Ramseyer, 1999). High Al and Fe in the hydrothermal quartz may reflect the enrichment of residual Al and Fe in the transitional aqueous phase. The bulk rock chemistry and the composition of melt inclusion within the magmatic quartz of the MQT are controversial. The chemical contrast between the melt inclusions and the MQT bulk rock demonstrate substantial mobility of K and Na during the evolution of the MQT. K and Na were separated from the MQT after solidification of magmatic quartz and prior to the crystallisation of the

hydrothermal quartz overgrowths. The high porosity of the MQT may correspond to the volume of lost constituents, which implies that these constituents escaped from the system when tourmaline and most of the quartz where almost solidified.

The difficulty in ascribing a magmatic or hydrothermal origin for the MQT is due, in part, to the problem of defining the state of systems during the transitional stages of magmato-hydrothermal evolution, especially if the system remains contained by impermeable wall-rocks. Late-stage magmatic systems contain a variety of immiscible phases, silicate melts, hydrous saline melts, aqueous fluids, and CO_2-rich vapours (Roedder, 1992). These complex phases, made up of both magmatic and hydrothermal components, are termed here 'transitional' (see above). In the strict sense, a hydrothermal phase already coexisted with the silicate magma during the FGG stage when an aqueous saline phase documented by melt inclusions, separated from the melt (Müller et al., submitted for publication). Clearly, the MQT started to crystallise from a highly evolved, boron-rich silicate melt containing a mixture of immiscible phases. Some of the phases together with the pre-enriched content of metals left the MQT system during solidification. Subsequent transport and deposition of Sn and Cu took place on departure of this vapour phase from the magmatic source, though the relationship between the MQT and tin and copper mineralisation is not always as intimate or direct as might be inferred. Residual aqueous phases flushed through residual porosity of the MQT resulting in overgrowths of hydrothermal quartz.

6. Summary

The evidence presented in this paper and elsewhere in the literature cited above shows that the SW part of the Land's End granite was formed by a complex sequence of intrusive events. Generally, three main stages of intrusion can be distinguished: (1) megacrystic fine-grained biotite (Mg-siderophyllite) granite (FGG), (2) megacrystic coarse-grained biotite (Mg-siderophyllite) granite (CGG), (3) fine- to medium-grained porphyritic and equigranular Li-siderophyllite granites. The main units form sub-horizontal granite sheets of 10- to 100-m-scale fed by dykes. The oldest biotite granite sheets (FGG) are entirely enclosed by

younger granites and form enclaves from cm- to 100-m-scale. Small batches and intrusions (<300 m) of tourmaline granite and MQT are mainly interpreted as differentiates of the Li-siderophyllite granites. Layers of tourmaline-rich granite also occur along the contacts of the biotite granites. The distinctive composition of the Li-mica-albite granite, the first albite granite to be described from the Land's End pluton, marks local evolution of a separate albite-rich melt from a relatively less-evolved source.

K-feldspar megacrysts within the older biotite granites (FGG and CGG) developed at an earlier stage of the evolution of the Land's End pluton. The intra-granular distribution of minor and trace elements from core to rim in the megacrysts reveals that crystallisation of the megacrysts took place in a moderately evolved magma. The element patterns of individual megacrysts indicate that the megacrysts crystallised in different magma batches, probably at different times. Rare plagioclase mantles around K-feldspar megacrysts are interpreted as having formed by nucleation of plagioclase on the K-feldspar surface as a result of local re-heating caused by mixing with different hotter batches of magma, accompanied by synneusis of plagioclase crystals at the K-feldspar surface under conditions of turbulent magmatic flow.

The younger intrusive units of the Land's End pluton are characterised by intense in situ fractionation and filter pressing, which led to concentration of boron in the apical parts of intrusive batches. The enrichment of the hydrous borosilicate phase and volatiles and their separation from the melt was an iterative process governed by the fractionation of the melt. The local co-existence of a saline aqueous phase with the silicate melt is demonstrated by melt inclusion assemblages, already providing evidence for the exsolution of halogen-bearing volatiles at the first stage of intrusion (FGG) of the Land's End pluton.

The tourmaline granites, which are interpreted as differentiates of the Pellitras granite and Li-siderophyllite granites, probably evolved large volumes of magmatic vapour which became the medium for metal transport and mineralisation in the St. Just mining district. The chemical contrast between the melt inclusions and the bulk rock of the MQT shows that alkalies were substantially mobilised during the transitional evolution of the MQT which contains textures indicative of this transitional magmatic stage. The MQT

crystallised mainly from a silica-rich melt and, to a lesser extent, from an aqueous fluid. The late-magmatic volatile enrichment and late- to post-magmatic fluid circulation is reflected in the strong alteration of accessory minerals within the MQT. The MQT is the final and barren product of phase immiscibility and separation during the transitional magmatic/hydrothermal stage is documented by compositional zoning of quartz and tourmaline and by melt inclusions. Transport and deposition of pre-enriched Sn and Cu from the magma took place within the hydrothermal system formed by emanation of the vapour phase from its source within the Li-siderophyllite granite and related tourmaline granites and MQT. This is inferred to be the origin of the 'emanative centre' underlying the St Just mining district which gave rise to the variety of hypothermal mineral lodes containing Sn, Cu and As.

Acknowledgements

Appendix A

A.1. Whole-rock geochemistry

Thirty-two representative samples from the Land's End pluton were selected for chemical analyses. Major and minor element analyses were determined by inductively coupled plasma atomic emission spectrometry (ICP-AES). Fluorine was separated by pyrohydrolysis and determined by ion chromatography. Cl was determined by the ion selective method.

ICP-MS measurements of the trace elements Rb, Sr, Y, Zr, Nb, Cs, Ba, Hf, Ta, Pb, U, Th, REE were made using an ELAN 5000A quadrupole ICP mass spectrometer (Perkin-Elmer/SCIEX, Canada) at the GeoForschungsZentrum (GFZ) in Potsdam. The procedure has been described in detail in Dulski (1994).

A.2. Electron probe microanalysis of minerals

The electron probe microanalyses of feldspar, mica, tourmaline, zircon, apatite and monazite were obtained using a Cameca SX50 microprobe at the Natural History Museum in London. The analyses were carried out using an accelerating voltage of 20 kV and beam currents of 20, 25 and 50 nA, respectively. The beam size used for zircon and monazite was 1 μm. The beam size was increased to 5 μm for feldspar, mica, and apatite to reduce beam-induced decomposition, and to prevent the migration of alkali elements. Interference corrections were made for Nd_2O_3, Sm_2O_3, Gd_2O_3 and Yb_2O_3 concentrations in monazite. A beam current of 50 nA was chosen for feldspar analyses. Alkalies were analysed first, which lead to a slight relative enrichment of Si during exposure to the electron beam because of the migration of alkalies. However, the loss of Na and K during feldspar analyses was not significant over the applied counting period of 10 s. Representative detection limits (3σ) for minor and trace elements in feldspar were 50 ppm for P, 61 for Ti, 129 for Fe, 176 for Sr, and 130 for Ba.

Analysis of tourmaline was carried out using a beam current of 25 nA and a spot size of ~5 μm. Detection limits (3σ of single point background) were 0.03 wt.% for MnO, MgO and TiO_2, 0.02 for CaO, 0.01 for K_2O and 0.09 for F. The data were recalculated to atoms per formula unit (apfu) based on 24.5 O, which assumes fixed B at 3 apfu and fixed (OH, F) at 4 apfu.

Abundances of the trace elements Al, K, Ti, and Fe in quartz were measured using a JEOL 8900 RL electron microprobe at the Geowissenschaftliches Zentrum Göttingen, Germany. For high precision and sensitivity, a beam current of 80 nA, a beam

diameter of 5 μm, and counting times of 15 s for Si, and of 300 s for Al, Ti, K, and Fe were chosen. Limits of detection (LOD) were (3σ of single point background) 60 ppm for Al, 18 ppm for K, 33 ppm for Ti, and 27 ppm for Fe.

A.3. Cathodoluminescence imaging

Scanning electron microprobe cathodoluminescence (SEM-CL) images were obtained using the JEOL 5900LV analytical SEM with an attached GATAN MiniCL detector.at the Natural History Museum in London The applied acceleration voltage and current was 20 kV and ~1 nA, respectively. The CL images were collected from 4 scans of 20 s and a processing resolution of 1280 by 960 pixels and 256 grey levels.Coloured cathodoluminescence images were captured using a NIKON FX-35A reflex camera attached to a hot-cathodoluminescence microscope (HC3-LM) at the Geowissenschaftliches Zentrum Göttingen using an acceleration voltage of 14 kV and a filament current of 0.18 mA. High-sensitivity KODAK Ektachrome 400 HC films were used.

A.4. LA-ICP-MS of feldspar

Laser ablation ICP-MS analyses of feldspar were carried out at the Natural History Museum in London using a New Wave Research UP213AI 213 nm aperture imaged laser ablation accessory coupled to a Thermo Elemental PQ3 ICP-MS. Operating condition for the laser and ICP-MS are given in Table 11. Samples were analysed along profiles from the core to the rim of K-feldspar megacrysts. K-feldspar megacrysts were analysed for the elements listed in Table 4. Elemental concentrations were calculated using NIST 612 reference material for calibration, Si was used for internal standardisation, its concentration at each analysis point having been determined by electron probe microanalyses adjacent to the ablation craters. The limit of detection (strictly limit of quantification) was taken as 10σ of the mean background count, and the data filtered at twice this limit (20σ). Examples of results are shown in Table 4. Accuracy was determined by analysing the USGS BCR2G basaltic glass material as an unknown and comparing this with reference values for BCR2 powder, in lieu of certified values for the fused BCR2G material. These analyses

Table 11
Operating conditions and parameters governing acquisition of analytical data during laser ablation ICP-MS analysis

ICP-MS	
Model	Thermo Elemental PlasmaQuad 3 with enhanced sensitivity 'S-option'
Forward power	1350 W
Gas flows:	
Coolant (plasma)	Ar: 13 l min^{-1}
Auxiliary	Ar: 0.8 l min^{-1}
Sample transport	He: ca. 1.1 l min^{-1}, Ar: ca 0.7 l min^{-1}
Laser	
Model	NewWave Research UP213 with aperture imaging
Wavelength	213 nm
Pulse width (FWHM)	3 ns
Pulse energy	0.05 mJ per pulse
Energy distribution	Homogenised, flat beam, aperture imaged
Energy density	3.5 J cm^{-2}
Focus	Fixed at surface
Repetition rate	10 Hz
Crater diameter	ca. 70 μm
Analysis protocol	
Scanning mode	Peak jumping, 1 point per peak
Acquisition mode	Time resolved analysis
Analysis duration	120 s, (ca 60 s background, 60 s signal)

showed that the LA-ICP-MS values are accurate within 3%.

References

Alderton, D.H.M., Sheppard, S.M.F., 1977. Chemistry and origin of thermal waters from southwest England. Transactions-Institution of Mining and Metallurgy. Section B. Applied Earth Science 86, 191–194.

Alderton, D.H.M., Pearce, J.A., Potts, P.J., 1980. Rare earth element mobility during granite alteration: evidence from southwest England. Earth and Planetary Science Letters 49, 149–165.

Badham, J.P.N., 1980. Late magmatic phenomena in the Cornish batholith—useful field guides for tin mineralisation. Proceedings of the Ussher Society 5, 44–53.

Behr, H.-J., Frentzel-Beyme, K., 1989. Permeability and paleoporosity in crystalline bedrocks of the Central European basement-studies of cathodoluminescence. In: Boden, A., Eriksson, K.G. (Eds.), Exploration of the Deep Continental Crust, Deep Drilling in Crystalline Bedrock, vol. 2. Springer, Berlin, pp. 477–497.

Bottrell, S.H., Yardley, B.W.D., 1988. The composition of a primary granite derived ore fluid from S.W. England, determined by fluid inclusion analysis. Geochimica et Cosmochimica Acta 52, 585–588.

British Geological Survey, 1984. Penzance. Sheet 351/358. Geological Maps of England and Wales, 1:50,000 Series.

Burns, P.C., MacDonald, D.J., Hawthorne, F.C., 1994. The crystal chemistry of manganese-bearing elbaite. Canadian Mineralogist 32, 31–41.

Candela, P.A., 1989. Calculation of magmatic fluid contributions to porphyry-type ore systems; predicting fluid inclusion chemistries. Geochemical Journal 23, 295–305.

Candela, P.A., Blevin, P.L., 1995. Do some miarolitic granites preserve evidence of magmatic volatile phase permeability? Economic Geology 90, 2310–2316.

Chang, L.L.Y., Howie, R.A., Zussman, J., 1996. Rock-Forming Minerals Volume 5B–non-silicates: Sulfates, Carbonates, Phosphates, Halides. Longman Group Limited, Essex. 383 pp.

Charoy, B., 1979. Définition et importance des phénomènes deutériques et des fluide associés dans les granites: conséquences métallogéniques. Sciences de la Terre (Nancy). Mémoires 37, 1–364.

Charoy, B., 1981. Post-magmatic processes in south-west England and Brittany. Proceedings of the Ussher Society 5, 101–115.

Charoy, B., 1982. Tourmalinization in Cornwall, England. In: Evans, A.M. (Ed.), Mineralization Associated with Acid Magmatism. John Wiley and Sons Ltd, London, pp. 63–70.

Charoy, B., 1986. The genesis of the Cornubian batholith (South-West England): the example of the Carnmenellis pluton. Journal of Petrology 27, 571–604.

Chen, Y., Clark, A.H., Farrar, E., Wasteneys, H.A.H.P., Hodgson, M.J., Bromley, A.V., 1993. Diachronous and independent histories of plutonism and mineralization in the Cornubian Batholith, southwest England. Journal of the Geological Society (London) 150, 1183–1191.

Chesley, J.T., Halliday, A.N., Snee, L.W., Mezger, K., Shepherd, T.J., Scrivener, R.C., 1993. Thermochronology of the Cornubian batholith in southwest England: implications for pluton emplacement and protracted hydrothermal mineralization. Geochimica et Cosmochimica Acta 57, 1817–1837.

Collins, J.H., Coon, J.M., 1914. On the topaz rock of St. Mewan Beacon, Cornwall. Transactions of the Royal Geological Society of Cornwall 15, 43–54.

Cox, R.A., Dempster, T.Y., Bell, B.R., Rogers, G., 1996. Crystallization of the Shap Granite: evidence from zoned K-feldspar megacrysts. Journal of the Geological Society (London) 153, 625–635.

Darbyshire, D.P.F., Shepherd, T.J., 1985. Chronology of granite magmatism and associated mineralization, SW England. Journal of the Geological Society (London) 142, 1159–1177.

Darbyshire, D.P.F., Shepherd, T.J., 1994. Nd and Sr isotope constraints on the origin of the Cornubian batholith, SW England. Journal of the Geological Society (London) 151, 795–802.

Davies, G., Gledhill, A., Hawkesworth, C., 1985. Nd and Sr isotope studies bearing on the crustal evolution of southern Britain. Earth and Planetary Science Letters 75, 1–12.

DePaolo, D.J., Linn, A.M., Schubert, G., 1991. The continental crustal age distribution: methods of determining mantle separation ages from Sm–Nd isotopic data and application to the southwestern United States. Journal of Geophysical Research 96, 2071–2088.

Dines, H.G., 1956. The metalliferous mining region of south-west England. Memoir of the Geological Survey of Great Britain. London, 2 volumes, 795 pp.

Dingwell, D.B., Knoche, R., Webb, S.L., Pichavant, M., 1992. The effect of B_2O_3 on the viscosity of haplogranitic liquids. American Mineralogist 77, 457–461.

Dingwell, D.B., Pichavant, M., Holtz, F., 1996. Experimental studies of boron in granitic melts. In: Grew, E., Anovitz, L. (Eds.), Boron, Mineralogy, Petrology and Geochemistry in the Earth's Crust, Reviews in Mineralogy, vol. 33, pp. 331–385.

D'Lemos, R.S., Kearsley, A.T., Pembroke, J.W., Watt, G.R., Wright, P., 1997. Complex quartz growth histories in granite revealed by scanning cathodoluminescence techniques. Geological Magazine 134, 459–552.

Dulski, P., 1994. Interferences of oxide, hydroxide and chloride analyte species in the determination of rare earth elements in geological samples by inductively coupled plasma-mass spectrometry. Fresenius' Journal of Analytical Chemistry 350, 194–203.

Eklund, O., Shebanov, A.D., 1999. Origin of the rapakivi texture by sub-isothermal decompression. Precambrian Research 95, 129–146.

Eliasson, T., Petersson, J., 1996. Deuteric accessory phases in the Bohus granite, SW Sweden. Geologiska Föreningens i Stockholm Förhandlingar 118, A12–A13.

Farmer, C.B., Halls, C., 1993. Paragenetic evolution of cassiterite-bearing lodes at South Crofty Mine, Cornwall, United Kingdom. In: Maurice, Y. (Ed.), Proceedings of the 8th Quadrennial IAGOD Symposium, Ottawa 1990. E. Schweizerbart'sche Verlagsbuchhandlung, Stuttgart, pp. 365–382.

Faye, G.H., Manning, P.G., Gosselin, J.R., Tremblay, R.J., 1974. The optical absorption spectra of tourmaline, cordierite, chloritoid and vivianite: ferrous–ferric electronic interaction as a source of pleochroism. American Mineralogist 53, 1174–1201.

Garnett, R.H.T., 1966. Relationship between tin content and structure of lodes at Geevor mine, Cornwall. Transactions-Institution of Mining and Metallurgy. Section B. Applied Earth Science 75, 1–22.

Gerstenberger, H., 1989. Autometasomatic Rb enrichments in highly evolved granites causing lowered Rb–Sr isochron intercepts. Earth and Planetary Science Letters 93, 65–75.

Goode, A.J.J., Taylor, R.T., 1988. Geology of the country around Penzance. Memoir of the British Geological Survey, Sheets 351 and 358 (England and Wales), HMSO, London. 51 pp.

Götze, J., Plötze, M., Habermann, D., 2001. Origin, spectral characteristics (CL) and practical applications of the cathodoluminescence (CL) of quartz—a review. Mineralogy and Petrology 71, 225–250.

Hall, A., 1990. Geochemistry of the Cornubian tin province. Mineralium Deposita 25, 1–6.

Halls, C., Jinchu, Z., Yucheng, L., 2002. Field evidence for discrete episodes of intrusion during the emplacement of the Land's End pluton. Results from detailed mapping and observation of the Porth Ledden coastal section. Proceedings of the Ussher Society 10, 221–222.

Hampton, C.M., Taylor, P.N., 1983. The age and nature of the basement of southern Britain: evidence from Sr and Pb isotopes

in granites. Journal of the Geological Society (London) 140, 499–509.

Harlov, D.E., Förster, H.-J., Nijland, T.G., 2002. Fluid-induced nucleation of (Y+REE)-phosphate minerals within apatite: nature and experiment: Part I. Chlorapatite. American Mineralogist 87, 245–261.

Hawkes, J.R., Dangerfield, J., 1978. The Variscan granites of SW England: a progress report. Proceedings of the Ussher Society 4, 158–171.

Hawkes, J.R., Harding, R.R., Darbyshire, D.P.F., 1975. Petrology and Rb:Sr age of the Brannel, South Crofty and Wherry elvan dykes, Cornwall. Bulletin of the Geological Survey of Great Britain 52, 27–42.

Hawthorne, F.C., Henry, D.J., 1999. Classification of the minerals of the tourmaline group. European Journal of Mineralogy 11, 201–215.

Heinrich, C.A., 1990. The chemistry of hydrothermal tin–tungsten ore deposition. Economic Geology 90, 705–729.

Hibbard, M.J., 1981. The magma mixing origin of mantled feldspar. Contributions to Mineralogy and Petrology 76, 158–170.

Hibbard, M.J., 1991. Textural anatomy of twelve magma-mixed granitoid systems. In: Didier, J., Barbarin, B. (Eds.), Enclaves and Granite Petrology, Developments in Petrology, vol. 13. Elsevier, Amsterdam, pp. 431–444.

Jackson, N.J., 1976. The Levant Mine Carbona, a fluid inclusion study. Proceedings of the Ussher Society 3, 427–429.

Jackson, N.J., 1977. The geology and mineralisation of the St. Just Mining District, West Cornwall. Unpublished PhD thesis, University of London. 408 pp.

Jackson, N.J., 1979. Geology of the Cornubian tin field: a review. Bulletin of the Geological Society of Malaysia 11, 209–237.

Jackson, N.J., Halliday, A.N., Sheppard, S.M.F., Mitchell, J.G., 1982. Hydrothermal activity in the St Just Mining District, Cornwall, England. In: Evans, A.M. (Ed.), Metallization Associated with Acid Magmatism. John Wiley and Sons Ltd, Londonp, pp. 137–179.

Kempe, U., Götze, J., 2002. Cathodoluminescence (CL) behaviour and crystal chemistry of apatite from rare-metal deposits. Mineralogical Magazine 66, 151–172.

Keppler, H., Wyllie, P.J., 1991. Partitioning of Cu, Sn, Mo, W, U, and Th between melt and aqueous fluid in the systems haplogranite–H_2O–HCl and haplogranite–H_2O–HF. Contributions to Mineralogy and Petrology 109, 139–150.

Larsen, R.B., 2002. The distribution of rare-earth elements in K-feldspar as an indicator of petrogenetic processes in granitic pegmatites: examples from two pegmatite fields in southern Norway. The Canadian Mineralogist 40, 137–151.

Leat, P.T., Thompson, R.N., Morrison, M.A., Henry, G.L., Trayhorn, S.C., 1987. Geodynamic significance of post-Variscan intrusive and extrusive potassic magmatism in SW England. Transactions of the Royal Society of Edinburgh. Earth Sciences 77, 349–360.

Lee, M.R., Parsons, I., 1997. Dislocation formation and albitization in alkali feldspars from the Shap granite. American Mineralogist 82, 557–570.

Lehmann, B., 1990. Metallogeny of Tin. Springer Verlag, Berlin. 211 pp.

Lehmann, B., Dietrich, A., Heinhorst, J., Métrich, N., Mosbah, M., Palacios, C., Schneider, H.-J., Wallianos, A., Webster, J., Winkelmann, L., 2000. Boron in the Bolivian tin belt. Mineralium Deposita 35, 223–232.

Liew, T.C., Hofmann, A.W., 1988. Precambrian crustal components, plutonic associations, plate environment of the Hercynian Fold Belt of Central Europe: indications from a Nd and Sr isotopic study. Contributions to Mineralogy and Petrology 98, 129–138.

Linnen, R.L., 1998. The solubility of Nb–Ta–Zr–Hf–W in granitic melts with Li and Li+F: constraints for mineralization in rare metal granites and pegmatites. Economic Geology 93, 1013–1025.

Linnen, R.L., Keppler, H., 2002. Melt composition control of Zr/Hf fractionation in magmatic processes. Geochimica et Cosmochimica Acta 66, 3293–3301.

London, D., Manning, D.A.C., 1995. Chemical variation and significance of tourmaline from southwest England. Economic Geology 90, 495–519.

Long, P.E., Luth, W.C., 1986. Origin of K-feldspar megacrysts in granitic rocks: implication of a partitioning model for barium. American Mineralogist 71, 367–375.

Ludwig, K.R., Silver, L.T., 1977. Lead-isotope inhomogeneity in Precambrian igneous K-feldspars. Geochimica et Cosmochimica Acta 41, 1457–1471.

Manning, D.A.C., 1981. The application of experimental studies in determining the origin of topaz–quartz–tourmaline rock and quartz–tourmaline rock. Proceedings of the Ussher Society 5, 121–127.

Manning, D.A.C., 1985. Comparison of the influence of magmatic water on the formation of granite-hosted Sn–W deposits and associated tourmalinisation from Thailand and S.W. England. In: Halls, C. (Ed.), High Heat Production (HHP) Granites, Hydrothermal Circulation and Ore Genesis, The Institution of Mining and Metallurgy Special Publication, pp. 203–212.

Mehnert, K.R., Büsch, W., 1981. The Ba content of K-feldspar megacrysts in granites: a criterion for their formation. Neues Jahrbuch für Mineralogie. Abhandlungen 140, 221–252.

Miller, C.F., Stoddard, E.F., Larry, J.B., Wayne, A.D., 1981. Composition of plutonic muscovites: genetic implications. Canadian Mineralogist 19, 25–34.

Mount, M., 1985. Geevor mine: a review. In: Halls, C. (Ed.), High Heat Production (HHP) Granites, Hydrothermal Circulation and Ore Genesis, The Institution of Mining and Metallurgy Special Publication, pp. 221–238.

Müller, B., Seward, T.M., 2001. Spectrophotometric determination of the stability of tin(II) chloride complexes in aqueous solution up to 300 degrees C. Geochimica et Cosmochimica Acta 65, 4187–4199.

Müller, A., Seltmann, R., Behr, H.J., 2000. Application of cathodoluminescence to magmatic quartz in a tin granite—case study from the Schellerhau Granite Complex, Eastern Erzgebirge, Germany. Mineralium Deposita 35, 169–189.

Müller, A., René, M., Behr, H.-J., Kronz, A., 2003a. Trace elements of igneous quartz in topaz granites from the Hub Stock (Slavkovský Les Mts., Czech Republic). Mineralogy and Petrology 79, 167–191.

Müller, A., Seltmann, R., Jeffries, T., Halls, C., 2003b. Late-Variscan rapakivi granites? Observations on the chemistry of plagioclase-mantled potassium feldspar phenocrysts. Berichte der Deutschen Mineralogischen Gesellschaft 15, 135.

Müller, A., Breiter, K., Seltmann, R., Pécskay, Z., 2005. Quartz and feldspar zoning in the eastern Erzgebirge volcano-plutonic complex (Germany, Czech Republic): evidence of multiple magma mixing. Lithos 80, 201–227.

Müller, A., Thomas, R., Wiedenbeck, M., Seltmann, R., Breiter, K., submitted for publication. Water content of granite and rhyolite melts from Cornwall and Erzgebirge: a Raman spectroscopy study of melt inclusions. European Journal of Mineralogy.

Mullis, J., Ramseyer, K., 1999. Growth related Al-uptake in fissure quartz, Central Alps, Switzerland. Terra Nostra 99 (6), 209.

Naumov, V.B., Karpukhina, E.N., Baranov, E.N., Konokova, N.N., 1999. Melt compositions, contents of volatile components and trace elements, and temperatures of quartz crystallization in silicic volcanic rocks of the Verkhneural'sk ore district (Southern Urals). Geochemistry International 37, 289–301.

Neiva, A.M.R., 1995. Distribution of trace elements in feldspars of granitic aplites and pegmatites from Alijó-Sanfins, northern Portugal. Mineralogical Magazine 59, 35–45.

Nekvasil, H., 1991. Ascent of felsic magmas and formation of rapakivi. American Mineralogist 76, 1279–1290.

Pichavant, M., 1979. Etude expérimentale à haute température et 1 kbar du rôle du bore dans quelques systèmes silicatés. Intérêt pétrologique et métallogénique. Thesis, Institut National Polytechnique de Lorraine Nancy. 153 pp.

Pichavant, M., 1981. An experimental study of the effect of boron on water-saturated haplogranite at 1 kbar pressure: geological applications. Contributions to Mineralogy and Petrology 76, 430–439.

Poitrasson, F., Chenery, S., Shepherd, T.J., 2000. Electron microprobe and LA-ICP-MS study of monazite hydrothermal alteration: implications for U–Th–Pb geochronology and nuclear ceramics. Geochimica et Cosmochimica Acta 64, 3283–3297.

Powell, T., Salmon, S., Clark, A.H., Shail, R.K., 1999. Emplacement styles within the Land's End Granite, Cornwall. Proceedings of the Ussher Society 9, 333–339.

Power, G.M., 1968. Chemical variation in tourmaline from Southwest England. Mineralogical Magazine 36, 1078–1089.

Pupin, J.-P., 2000. Granite genesis related to geodynamics from Hf–Y in zircon. Transactions of the Royal Society of Edinburgh. Earth Sciences 91, 245–256.

Raimbault, L., Cuney, M., Azencott, C., Duthou, J.L., Joron, J.L., 1995. Geochemical evidence for a multistage magmatic genesis of Ta–Sn–Li mineralization in the granite at Beauvoir, French Massif Central. Economic Geology 90, 548–576.

Ramseyer, K., Mullis, J., 1990. Factors influencing short-lived blue cathodoluminescence of α-quartz. American Mineralogist 75, 791–800.

Roedder, E., 1992. Fluid inclusion evidence for immiscibility in magmatic differentiation. Geochimica et Cosmochimica Acta 56, 5–20.

Salmon, S., 1994. Mingling between coexisting granite magmas within the Land's End Granite—preliminary observations. Proceedings of the Ussher Society 8, 219–223.

Salmon, S., Powell, T., 1998. Variation in the fine-grained granites of the Land's End pluton. Proceedings of the Ussher Society 9, 157–164.

Salmon, S., Shail, R.K., 1999. Field excursion to examine the granites in the area between Cape Cornwall and Porth Nanven, West Penwith, 3rd January 1999. Proceedings of the Ussher Society 10, 391–393.

Schleicher, H., Lippolt, H.J., Raczek, I., 1983. Rb–Sr systematics of Permian volcanites in the Schwarzwald: Part II. Age of eruption and the mechanism of WR age distortion. Contributions to Mineralogy and Petrology 84, 281–291.

Shackleton, R.M., Ries, A.C., Coward, M.P., 1982. An interpretation of the Variscan structures in SW England. Journal of the Geological Society (London) 139, 533–541.

Shail, R.K., Stuart, F.M., Wilkinson, J.J., Boyce, A.J., 2003. The role of Post-Variscan extensional tectonics and mantle melting in the generation of lower Permian granites and the giant W–As–Sn–Cu–Zn–Pb orefield of SW England. Transactions-Institution of Mining and Metallurgy. Section B. Applied Earth Science 112, 127–129.

Sheppard, S.M., 1977. The Cornubian batholith, S.W. England: D/H and $^{18}O/^{16}O$ studies of kaolinite and other alteration minerals. Journal of the Geological Society (London) 133, 573–591.

Shinohara, H., Iiyama, J.T., Matsuo, S., 1989. Partition of chlorine compounds between silicate melt and hydrothermal solutions: I. Partition of NaCl–KCl. Geochimica et Cosmochimica Acta 53, 2617–2630.

Smith, J.V., 1983. Some chemical properties of feldspars. In: Ribbe, P.H. (Ed.), Feldspar Mineralogy, 2nd edition. Reviews in Mineralogy, vol. 2, pp. 281–296.

Sprunt, E.S., Nur, A., 1979. Microcracking and healing in granites: new evidence from cathodoluminescence. Science 205, 495–497.

Stimac, J.A., Clark, A.H., Chen, Y., Garcia, S., 1995. Enclaves and their bearing on the origin of the Cornubian batholith, southwest England. Mineralogical Magazine 59, 273–296.

Stone, M., 2000. Petrogenetic implications from biotite compositional variations in the Cornubian granite batholith. Mineralogical Magazine 64, 729–735.

Stone, M., Exley, C.S., 1984. Emplacement of the Porthmeor granite pluton, West Cornwall. Proceedings of the Ussher Society 6, 42–45.

Taylor, J.C., Wall, V.J., 1993. Cassiterite solubility, tin speciation, and transport in magmatic acqueous phase. Economic Geology 88, 437–460.

Tischendorf, G., Förster, H.-J., Gottesmann, B., 2001. Minor- and trace-element composition of trioctahedral micas: a review. Mineralogical Magazine 65, 249–276.

Valley, J.W., Graham, C.M., 1996. Ion microprobe analysis of oxygen isotope ratios in quartz from Skye granite: healed micro-cracks, fluid flow, and hydrothermal exchange. Contributions to Mineralogy and Petrology 124, 225–234.

Vance, J.A., 1969. On synneusis. Contributions to Mineralogy and Petrology 24, 7–29.

Van Marcke de Lummen, G., 1986. Geochemical variation of the Land's End granite (south-west England) in relation to its tin

potential in the light of data from western marginal areas. Proceedings of the Ussher Society 6, 398–404.

Ward, C.D., McArthur, J.M., Walsh, J.N., 1990. Rare earth element behaviour during evolution and alteration of the Dartmoor granite, SW England. Journal of Petrology 33, 785–815.

Wark, D.A., Stimac, J.A., 1992. Origin of mantled (rapakivi) feldspars: experimental evidence of a dissolution- and diffusion-controlled mechanism. Contributions to Mineralogy and Petrology 111, 345–361.

Watson, J.V., Fowler, M.B., Plant, J.A., Simpson, P.R., 1984. Variscan–Caledonian comparisons: late orogenic granites. Proceedings of the Ussher Society 6, 2–12.

Watt, G.R., Wright, P., Galloway, S., McLean, C., 1997. Cathodoluminescence and trace element zoning in quartz phenocrysts and xenocrysts. Geochimica et Cosmochimica Acta 61, 4337–4348.

Williamson, B.J., Spratt, J., Adams, J.T., Tindle, A.G., Stanley, C.J., 2000. Geochemical Constraints from zoned hydrothermal tourmalines on fluid evolution and Sn mineralisation: an example from Fault breccias at Roche, SW England. Journal of Petrology 41, 1439–1453.

Wilson, I.R., 1972. Wallrock alteration at Geevor Mine. Proceedings of the Ussher Society 2, 425–434.

Wilson, I.R., Floyd, P.A., 1974. Distribution of uranium in the Land's End granite and aureole and various greenstones from Cornwall. Proceedings of the Ussher Society 3, 166–176.